

Remote sensing of local-dust across the Canadian Arctic

Seyed Ali Sayedain¹, Norman T. O'Neill¹, Keyvan Ranjbar², Phillippe Gauvin-Bourdon³, Rachel Chang³, Patrick L. Hayes⁴, James King⁵

¹Centre d'Applications et de Recherches en Télédétection, Université de Sherbrooke, Sherbrooke, QC, Canada

²Flight Research Laboratory, National Research Council Canada, Ottawa, ON, Canada

³Department of Physics and Atmospheric Science, Dalhousie University, Halifax, NS, Canada

⁴Département de chimie, Université de Montréal, Montréal, QC, Canada

⁵Département de géographie, Université de Montréal, Montréal, QC, Canada

Correspondence to: S. A. Sayedain (seyed.ali.sayedain@usherbrooke.ca)

Abstract.

We investigated the optical and microphysical characterization of High- and sub-Arctic dust events across the Canadian Arctic Archipelago (CAA). Events from local sources (local dust) were first identified and characterized using a combination of ground-based lidar, two AERONET instruments, and passive (MODIS, Sentinel-2, MISR) imagery in the neighbourhood of the High-Arctic Polar Environment Atmospheric Research Laboratory (PEARL) at Eureka, Nunavut (on Ellesmere Island in the northernmost part of the CAA).

The PEARL findings informed the identification and characterization of local dust events over other parts of the CAA using a suite of satellite instruments whose remote sensing (RS) capabilities were complementary to or an extension of the ground- and satellite-based techniques employed at Eureka. The events included plumes emanating from Axel Heiberg Island, just west of Ellesmere Island, Banks Island in the southwest corner of the CAA, Ellef Ringnes Island in the eastern part of the central CAA and Prince of Wales Island / Victoria Island in the central southern CAA. Plume identification, plume source and CM (coarse mode) aerosol optical depth (AOD) retrievals were investigated using a combination of low to high spatial resolution (MODIS to Sentinel-2) color imagery and the MODIS dark target AOD product over water. Plume thickness, height and speed for most of the events were obtained (depending on orbit availability and lack of cloud contamination) from MISR (Multi-angle Imaging Spectro Radiometer) stereoscopic products.

These RS results support an argument for the ubiquitous presence of pan-Arctic, low altitude dust that is typically (away from any strong sources such as mountainous drainage basins) at the lower levels of detectability offered by ground- and satellite-based RS techniques. The ability to RS airborne, near-source, local dust events and characterize dust properties and dynamics of important regions such as the CAA is critical to understanding local dust impacts such as early snow/ice melt and the nucleation role of local dust in the formation of low-altitude clouds.

30 **1 Introduction**

31 Local, drainage-flow dust events are recognized as an important source of dust at high latitudes (Bullard et al., 2016) and are
32 a significant contributor to Arctic and sub-Arctic aerosols in terms of total atmospheric (columnar) dust loads and notably, to
33 near-surface concentration and attendant surface deposition (Groot Zwaaftink et al., 2016). Meinander et al. (2022) employed
34 dust-transport simulations supported by recent verification data (including the identification of sources using satellite-based
35 imagery) to confirm the predominance of high-latitude dust (HLD) sources in terms of snow and ice deposition. O'Neill et al.
36 (2025) summarized satellite-derived findings of what was likely local dust deposition (with attendant decreases in visually
37 observed surface reflectance) for a sampling of drainage basin regions in the CAA. Local dust, whose source plumes can
38 produce quite strong coarse mode¹ (CM) AODs (aerosol optical depths) eventually spread out and/or are deposited to yield
39 weak, monthly-binned CM AODs (O'Neill et al., 2025 who employ the term DOD [dust optical depths] for the CM AODs
40 known to be dominated by dust).

41 Dust from Asian deserts can be transported around the world and contributes to the dust load over the Arctic (see for example
42 Uno et al., 2009). AboEl-Fetouh et al. (2020) argued that there was a small but distinct springtime, pan-Arctic (CM) AOD²
43 contribution of what was likely Asian dust over six AERONET stations spread across the Canadian and northern European
44 Arctic. They also noted that the particle-volume size distribution (PVSD) associated with those CM AODs showed a peak
45 radius $\sim 1.3 \mu\text{m}$. This feature tends to dominate monthly-binned CM AOD averages in the spring (ibid) while DODs associated
46 with local sources are likely more prevalent in the summer and fall according to the monthly-binned simulations (Fig. 7) of
47 Groot Zwaaftink et al. (2016)³. Aside from its rather unique temporal signature, Asian dust tends to be concentrated in weak
48 to moderately strong DOD plumes located in the mid- to upper-troposphere with some evidence of dust deposition during the
49 period of relatively strong Asian dust events (see, for example, the Fig. 3 Barrow event of Zhao et al., 2022).

50 Local dust particles in the Arctic are known to be strong ice nucleating particles (INPs) that can significantly influence the
51 dynamics of mixed-phase clouds (ice crystals and water droplets) and their optical and radiative impacts (Xi et al., 2022, Kawai
52 et al., 2023). The dust plumes lofted into the atmosphere from the Copper River Delta in southern Alaska during late summer
53 or autumn were, for example, shown to be a major INP source (Barr et al., 2023). Those authors also pointed out that the dust
54 events can last for many days and extend hundreds of kilometers into the Gulf of Alaska. Tobo et al. (2019) noted that the high
55 ice nucleating ability of local dust in the Svalbard region of the European Arctic was likely improved by the presence of organic
56 matter.

¹ Roughly speaking, particles of super μm (radius) size

² their CM AODs corresponded to integrations of the retrieved AERONET particle-volume size distribution across retrieval radii ranging from a fixed (interpolated) value of $0.6 \mu\text{m}$ (Dubovik et al., 2002) to an upper bin edge of $17.18 \mu\text{m}$ (AboEl-Fetouh et al., 2020 explicitly define the bin centers and the bin edges in their Table S1)

³ Their source and receptor regions represent broad "cap" areas that are greater than a certain latitude

57 HLD events in the Canadian Arctic and specifically the CAA are rarely monitored and so their properties are, accordingly, not
58 well characterized: low population density and limited numbers of meteorological stations have resulted in a scarcity
59 of observations. Persistent cloudy periods and the attendant underuse of RS data have represented significant challenges to the
60 exploitation of satellite RS data (Bullard et al., 2016). Alternatively, optically thinner clouds and / or surface reflectance
61 perturbations (such as white froth from waves) could act to contaminate AOD retrievals over water.

62 Satellite imagery at different spatial and temporal resolutions in the polar regions can provide color images of dust events as
63 well as plume characterization products (including AOD, plume height and thickness, coarse indicators of particle size,
64 etc.) that help to better characterize local dust. Satellite-based, high spatial-resolution RS data can, for example, enable the
65 separation of local dust-plume patterns from suspended sediments and phytoplankton blooms in the water.

66 The identification of dust plumes over the Icelandic region using MODIS true color imagery has been reported for events
67 dating back to 2002 (Arnalds, 2010). Satellite- and airborne-RS of local dust over the Arctic (as summarized by Sayedain et
68 al., 2023; SDN) include airborne RS of dust over the riverbed, fjord, and coastal regions of Svalbard, sub-Arctic dust plumes
69 flowing over the Gulf of Alaska (where they are much more readily identified and characterized), and MODIS- and CALIOP-
70 based identification of dust plumes from Iceland. A local, high-Arctic CM dust plume, induced by the drainage basin dynamics
71 of Lake Hazen (~ 300 km northeast of Eureka on Ellesmere Island), was identified and characterized by Ranjbar et al. (2021)
72 using various types of passive and active, satellite-based RS tools adapted to the special case of dust optics and microphysics.
73 Baddock et al. (2024) provided a detailed analysis of a dust event over Pearly Land, Northern Greenland employing Sentinel-
74 2 true-color images supported by reanalyzed near-surface wind and temperature data.

75 In terms of ground-based RS, Yang et al., (2020) used Doppler lidar (backscatter and depolarization ratio channels) and
76 ceilometer profiles, along with CIMEL photometry (the instrument employed by AERONET) to characterize the optical
77 properties of Icelandic, sub-Arctic dust plumes. Bachelder et al. (2020) reported peak CM radii of ~ 1.63 μm for their measured
78 near-source particle-mass size distributions (PMSDs) of local dust in the sub-Arctic Ä'äy Chù (Slims River) basin in the
79 Canadian Yukon. SDN characterized the optical and microphysical properties of Lhù'ààn Mân⁴ dust plumes using CIMEL
80 and Doppler lidar instrumentation supported by microphysical surface measurements. Their CIMEL- and lidar-derived dust
81 AODs (which we will refer to as DODs in cases where dust is likely the predominant aerosol) were CM dominated (~~be~~-weaker
82 fine mode DODs that correlated with the CM DODs were also observed).

83 Kawai et al. (2023) simulated the columnar mass concentrations of local dust in the Arctic in order to lay the groundwork for
84 their investigations into the strong role of local dust as INP. They employed CALIOP profiles and the CALIOP aerosol subtype
85 classification product to produce a local-dust Arctic DOD climatology in order to verify the quality of their dust simulations.
86 Their map of simulated columnar mass abundance of pan-Arctic dust (~~and its conversion to CM DODs at 550 nm as per~~
87 ~~O'Neill et al., 2025~~)-helped contextualize (roughly guide or even semi-quantitatively validate) our search for dust events in

⁴ The Kluane Lake Research Station about 8 km east of the Ä'äy Chù measurement station

88 the CAA that would be detectable using satellite-based RS. In general, we expect DODs associated with local dust to be
89 dominated by CM particles (see, for example, the overview given in O'Neill et al., 2025).
90 The instruments and measurements that we employed in the investigations reported in this paper, reflect a general strategy of
91 using ground-based microphysical as well as ground-based passive and active RS measurements acquired at the High-Arctic
92 PEARL observatory as a means of demonstrating the presence of local dust in the PEARL region and then linking, by direct
93 or indirect means, this information with imagery ~~and lidar RS products~~ available from the very frequent overpasses of satellite-
94 based instruments over a site that is ~~very~~-near the tangent circle of all polar-orbiting satellites (and thus the beneficiary of a
95 high density of RS data). With this type of analysis in hand we sought to support/inform (without the ground-based RS and
96 microphysical sampling capabilities of the PEARL complex), the purely satellite-based RS and characterization of local dust
97 events in other parts of the CAA. The motivation for this work was to analyze and help verify / evaluate elements of the large
98 potential trove of satellite-based dust RS data over the CAA.

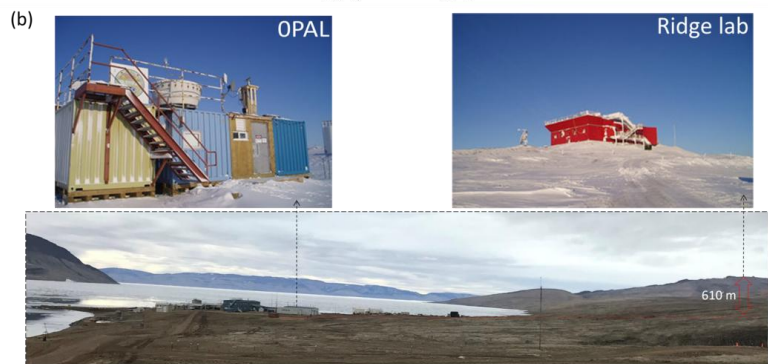
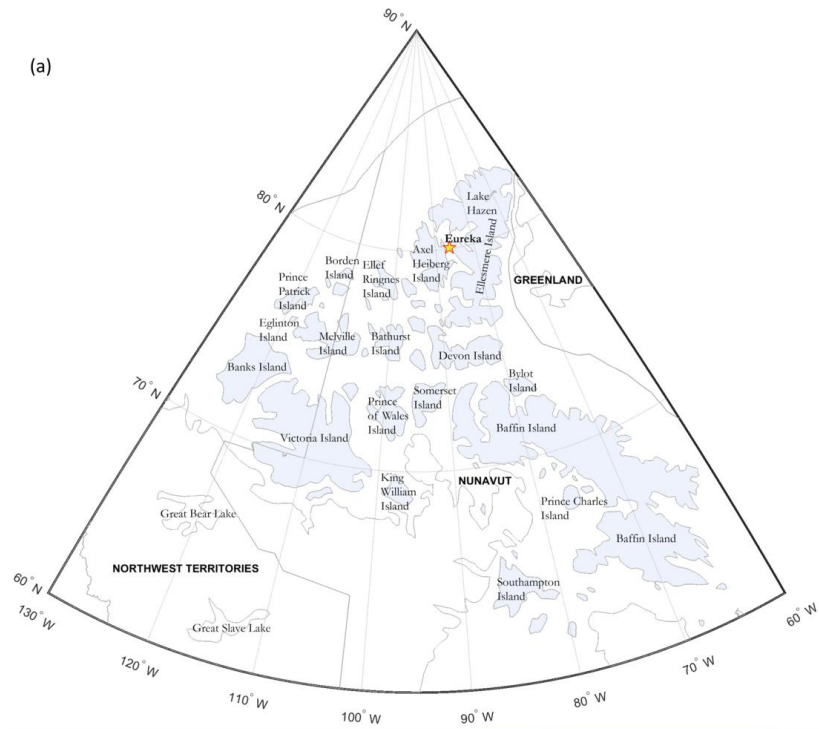
99 **2 Study Area**

100 **2.1 The Canadian Arctic Archipelago**

101 The CAA extends from the northern (low Arctic) shores of the Canadian mainland to the high Arctic ~~near the North Pole~~ (Fig.
102 1a). It consists of a group of approximately 36,000 islands, many of which are covered by ice for much of the year (Adams et
103 al., 2015). Different local CAA dust events at Eureka on Ellesmere Island, Axel Heiberg Island, Prince of Wales Island, Banks
104 Island, and Ellef Ringnes Island were investigated as part of this local dust analysis.

105 **2.1.1 The PEARL research complex**

106 The Polar Environment Atmospheric Research Laboratory (PEARL) at Eureka is an important High-Arctic location where
107 optical and microphysical measurements of gases, aerosols and clouds are conducted on a quasi-continuous basis. The PEARL
108 complex (indicated by a star on the map of Fig. 1a) includes two atmospheric measurement sites (Fig. 1b): the OPAL (Zero
109 Altitude PEARL Auxiliary Laboratory) at 5 m ASL, and the Ridge lab at 615 m ASL. ~~A 3rd measurement site known as
110 SAFIRE (Surface and Atmospheric Flux, Irradiance and Radiation Extension) is located about 5 km from OPAL.~~ The OPAL
111 site and the Ridge lab are separated by a 15 km-long gravel road.



113 Figure 1 – (a) The geographical extent of the CAA as indicated by light-blue shading. The PEARL observatory at Eureka, Nunavut
114 is indicated by a yellow star, (b) the PEARL complex showing both the 0PAL (left) and Ridge lab (right) sites (a wide-angle photo
115 of the PEARL complex is below those photos). The nominal (AERONET) coordinates of the 0PAL and Ridge lab sites are,
116 respectively; 79.990° N, 85.939° W at 5 m elevation and 80.054° N, 86.417° W at 615 m elevation.

117 3 Instrumentation & Methodology

118 In this section, we present a brief overview of the instruments and measurements employed in our local dust investigations at
119 the PEARL complex and a summary of the satellite imagery products that we employed over targeted CAA sites in our search
120 for detectable dust events.

121 3.1 Sun photometer / sky radiometer

122 Spectral AOD and almucantar sky radiance measurements were acquired by two automated AERONET CIMEL sun
123 photometer/sky radiometers (see Giles et al., 2019, for recent details on the CIMEL instrument and the AERONET network).
124 The Canadian sub-network of AERONET (AEROCAN) is run by Environment and Climate Change Canada (ECCC) in
125 collaboration with AERONET (Ihab Abboud is the AEROCAN coordinator). The Ridge lab and the 0PAL CIMEL have been
126 in operation from 2007 to 2019 and from 2007 to the present, respectively⁵. The Ridge lab CIMEL is labeled "PEARL" in the
127 AERONET database.

128 The CIMEL instruments acquire solar-disk irradiances across eight spectral channels from the ultraviolet (UV) to the short-
129 wave infrared (SWIR) at central wavelengths (λ) of 340, 380, 440, 500, 675, 870, 1020, and 1640 nm in a sequence of three
130 10-second (triplet) observation at a nominal temporal resolution of 3 minutes between triplets (15 min for older CIMEL
131 versions). Version 3, Level 1.0 AERONET AODs were employed in the analysis (unless otherwise stated). These AOD spectra
132 yield fine mode (FM) and coarse mode (CM) AODs (the AERONET SDA product at 500 nm wavelength) with pre-cloud-
133 screened filtering being driven by a ceiling on the variation of the triplets (see Giles et al., 2019, for AERONET processing
134 details and products) .

135 The CIMELs also acquire (low frequency) AOD spectra and almucantar radiances across four spectral bands (380, 440, 675,
136 870 nm) at a nominal temporal resolution of 1 hour⁶. Version 3, Level 1.5 (cloud-screened) AOD measurements and associated
137 almucantar radiances are inverted to yield (what amount to) columnar averages of refractive index and PVSDs.

⁵ The AERONET database name for "0PAL" is written as "OPAL"

⁶ supplemented by 4 additional AOD / almucantar measurement series at solar airmasses of 4, 3, 2 and 1.7 (Sinyuk et al., 2020).

138 3.2 Aerodynamic Particle Sizer Spectrometer

139 The Aerodynamic Particle Sizer (APS) spectrometer measures both aerodynamic diameter and light-scattering intensity (TSI
140 Incorporated, 2022). Their basic size distribution product is a largely CM product (52 optical channels with an aerodynamic
141 particle diameter range between 0.5 to 20 μm). The chosen temporal bin-sampling frequency was 1 minute. Particle-number
142 size distributions ($dN/d\log D$) are calculated by dividing the measured number concentration of each bin by its logarithmic
143 bin size ($d\log D$). PVSD concentrations ($dv/d\log D$) are then expressed in terms of equivalent spherical particles
144 ($\frac{4}{3}\pi (D/2)^3 dN/d\log D$). CM particle-volume concentrations (v_c) are obtained by adding the $dv = PVSDs \times d\log D$ across
145 a range of CM channels⁷ ($v_c = \sum_{i=21}^{i=52} dv$).

146 3.3 Arctic High Spectral Resolution Lidar

147 The Arctic High Spectral Resolution Lidar (AHSRL) was deployed at OPAL between August 2005 and June 2010. The AHSRL
148 employs Doppler-type lidar technology to separate (slow-moving aerosol and fast-moving molecular), velocity-induced
149 differences in Doppler frequencies. This separation enables the retrieval of particle (aerosol and/or cloud) to molecular
150 backscatter coefficient ratios that, in turn, allow for the extraction of particle backscatter profiles by the simple expediency of
151 multiplying by the relatively well-known molecular backscattering profile (see Eloranta's HSRL chapter in Weitkamp, 2005).
152 The AHSRL provides backscatter coefficient⁸ (β with units of $\text{sr}^{-1} \text{km}^{-1}$) and volume depolarization ratio (VDR⁹) profiles of 7.5
153 m vertical resolution up to 30 km of altitude and inter-sample resolution of 1 minute (Eloranta et al., 2004). The VDR is a
154 well-known source of information related to the optical separation of FM and CM contributions to the backscatter signal. We
155 employ that type of information below to make links with CM AODs (DODs) derived from the CIMEL instruments.

156 The β altitude profiles can be integrated to yield what we refer to as the particulate backscatter optical depth (τ_β) whose FM
157 and CM AOD components are $\tau_{\beta,f}$ and $\tau_{\beta,c}$. If the FM and CM profiles are largely dominated by homogeneous particle types
158 (like, respectively, FM sulphatic-based pollution particles and CM dust) then their corresponding optical depths are given by
159 $\tau_f^l = S_f \tau_{\beta,f}$ and $\tau_c^l = S_c \tau_{\beta,c}$ (where S_f and S_c are the lidar ratios [sr] of the FM and CM particle types).

⁷ from bin (i) = 21 to 52. This bin range corresponds to geometric bin center diameters of $D = 1.47$ to $13.66 \mu\text{m}$. Geometric diameters are taken as the aerodynamic diameter / 1.45 (see, for example, Huang et al., 2021).

⁸ What the lidar community refers to as backscatter cross section (but which we have adapted to better fit into the extinction coefficient vocabulary of the radiative transfer community; see, for example, Hansen and Travis, 1974)

⁹ For purposes of symbolic brevity, we also employ δ to represent VDR in any equation context.

160 **3.4 Satellite imagery**

161 MODIS satellite images along with their derived AOD products as well as MISR multi-view images and their AOD, plume
162 height and plume speed products were employed to investigate a variety of dust events using the contextualizing diversity of
163 information layers available from the NASA Worldview¹⁰ application. High spatial resolution Sentinel-2 color images from
164 the Copernicus Browser¹¹ were also employed on an as-needed basis: they often yielded physical and/or spatio-temporal
165 insights into local dust behavior that was not obvious in the (comparatively) low-resolution MODIS imagery and products.

166 **3.4.1 MODIS**

167 MODIS multispectral imagers operate on both the descending-orbit (Terra) and ascending orbit (Aqua) satellites at an altitude
168 of 705 km¹². MODIS employs 36 spectral bands between 400 nm (UV) and 14.4 μm (thermal-IR) at three different nadir
169 spatial resolutions of 250 m (bands 1–2), 500 m (bands 3–7), and 1 km (bands 8–36). The sensor has a swath width of 2330
170 km (cross-track) by 10 km (along track at nadir) and views the entire Earth every one to two days, depending on the latitude
171 of the orbit line (Justice et al., 2002). The MODIS “true color” RGB images provided by the NASA Worldview application
172 have a spatial resolution of 250 m (R = Band 1 @ 620–670 nm, G = Band 4 @ 545–565 nm, B = Band 3 @ 459–479 nm).

173 The highest-resolution, 3 km land and ocean (550 nm) AOD products (Terra, MOD04_3K, and Aqua,
174 MYD04_3K) are computed using the Dark Target (DT) algorithms over dark land and ocean targets during daytime overpasses
175 (Levy et al. 2015a, 2015b). We employed the 3 km data while monitoring the predictions of the 10 km Deep Blue (DB) AOD
176 product over Arctic land surfaces (Levy et al. 2015c, 2015d) where the DT AOD product was typically sparse or non-existent.
177 The DT algorithm’s dependence on the presence of dense dark vegetation to achieve its dark pixel threshold over land is rarely
178 achieved over the Arctic: the DB algorithm was designed to retrieve AOD over surfaces such as deserts or arid lands that are
179 bright in the visible wavelength spectrum (Sayer et al., 2014). It is tempting to employ this product given that vegetation-
180 sparse Arctic tundra often satisfies the conditions for the generation of DB AODs. However, it is a largely untested product
181 over high-Arctic sites (Sayer, 2025) and our investigations showed the presence of frequent AOD plumes (patches) that were
182 often inordinately coincident with persistently dark reflectance patterns in the imagery. In the end we relied almost exclusively
183 on the DT retrieval over water surfaces.

184 We employed the MODIS FMF (Fine Mode Fraction) product (Song et al., 2021) as a means of separating out the CM AOD
185 from the AOD (CM AOD = (1 – FMF) × AOD). As indicated above, the DOD is generally expected to be dominated by CM
186 particles. [Sea-spray particles are also CM in nature: however, the unique spatial nature of dust plumes and their land-based
187 origin largely occluded any possible mixup with sea-salt particles.](#)

¹⁰ <https://worldview.earthdata.nasa.gov/>

¹¹ <https://dataspace.copernicus.eu/browser>

¹² Local-time equatorial crossings of 10:30 a.m. and 1:30 p.m. respectively

3.4.2 MISR

The Multi-angle Imaging SpectroRadiometer (MISR), aboard the Terra satellite, acquires images of the same scene at nine different viewing angles. The imagery is obtained at angles ranging from aft- or backward-looking (-70°) to fore- or forward-looking ($+70^\circ$) views in four spectral bands (blue @ 447 nm, green @ 558 nm, red @ 672 nm, and near-infrared @ 867 nm). The “Global Mode” nadir spatial resolution is 275 m which degrades to 1.1 km for all off-nadir bands except the red band (MISR Handbook, 2000). The latitude-dependent revisit time is every 2 to 9 days (depending on latitude) across a 380 km swath (Garay et al., 2020). The stereoscopic nature of the 9 MISR images enables the extraction of plume height and plume velocity. Both parameters are critical for dust plume investigations. This was notably demonstrated by Ranjbar et al. (2021), for the case of a strong local-dust plume over Lake Hazen (about 330 km northeast of PEARL) that was characterized using MISR, MODIS, CALIOP and CloudSat data. More detailed information on MISR stereoscopic height and wind speed retrievals and the algorithm used to generate these products (the MISR Interactive eXplorer or MINX algorithm) can be found in Nelson et al. (2013), who also provide case studies of plume height and wind speed retrievals for smoke, dust, and cloud. It was known, from its earliest conception, that the multi-angle feature of MISR would facilitate the extraction of aerosol parameters given their spatial invariance¹² relative to the typically high frequency spatial variance and differing spectra of surface reflectance (see, for example, the definitive overview of Martonchik et al., 1998). The specific stereoscopic capabilities of MISR enable, in turn, the detection of aerosol or cloud plumes and the computation of their optical depth (see, for example, Kahn et al., 2007, for the case of dust, smoke and volcanic plumes at the 17.6 km atmospheric processing resolution). More recent versions of the MISR processing chain included a 4.4 km resolution, near real time, V23, Level 2 AOD product (Witek et al., 2021) whose AODs are reported at the standard reference wavelength of 550 nm (ibid). We employed both the MISR plume height and AOD products in our investigations of local-dust events across the CAA.

Commented [NO1]: This is repeated in the sentence below

4 Results & Discussion

Our results are reported in two subsections: 4.1- Analysis of dust events at Eureka ~~Ground-based RS and microphysical analysis at Eureka with links to satellite-based RS imagery over that site~~, and 4.2- Satellite-based RS of local dust events across the CAA ~~Satellite-based RS of local dust events across the CAA~~. Our goal is to demonstrate how an experienced-based local dust narrative can be built using the ground-based optical and microphysical measurements of dust plumes in the Eureka region while underscoring what can be achieved using satellite-based RS data ~~that is~~ informed, as much as possible, by the ground-based and satellite-based results at Eureka.

¹²across initial atmospheric processing pixels of 17.6 km resolution

215 4.1 Analysis of dust events at Eureka

216 We carried out a purely optical analysis comparing CIMEL and AHSRL data¹⁴ in order to ~~demonstrate~~-investigate certain
217 optical dynamics that were consistent with the apparent presence of dust particles at low elevations between OPAL and the
218 Ridge lab. In a different sequence of aerosol events, the OPAL CIMEL AOD measurements and in situ APS PVSDs shared a
219 common measurement period from July 9 to September 20, 2018. These two periods were an important focus of our ground-
220 based analysis at the PEARL sites. The correlation between different independent datasets was a key aspect of a multi-pronged
221 strategy to provide evidence of Arctic dust events whose RS detectability can be generally characterized as weak to marginal
222 (O'Neill et al., 2025).

223 4.1.1 Passive vs active (ground-based) optical analysis at Eureka

224 Potential dust events over ~~the the-August—2005 to June 2010~~ period ~~from August-2005 to June 2010~~ (the duration of AHSRL
225 measurements at OPAL) were investigated by looking for low-altitude, large-amplitude VDR events whose derived CM ~~optical~~
226 ~~depths~~AODs were correlated with the OPAL CM AOD (τ_c^o) and not correlated with the PEARL CM AOD (τ_c^p) (if the plumes
227 were found to be largely below the PEARL ~~CIMEL CIMEL~~-elevation of 615 m). The AHSRL CM AODs (τ_c^l) were obtained
228 by integrating ~~CM lidar backscatter coefficient~~ (β_c) profiles associated with VDR values greater than a particular threshold
229 (δ_{thr}) (from ~~5 to 615 m~~ (the OPAL to Ridge lab elevations)) and employing prescribed FM and CM lidar ratios. The reader is
230 directed to Appendix A1 for a discussion of the FM / CM attributions between the OPAL and PEARL CIMELs and for temporal
231 resampling details (the resampling of τ_c^p and τ_c^l measurements to τ_c^o times). The theoretical VDR-driven FM / CM attributions
232 for the lidar ~~optical depths~~ are defined in Appendix A2.

233 We analyzed the AHSRL profile statistics of 7 ~~potential events that we claimed to be~~ dust events in Section A3.2. The impact
234 of varying the FM / CM attribution threshold of the VDRs (the value of δ_{thr}) is detailed in Appendix A3.3¹⁵. We eventually
235 determined that a 5% VDR threshold for separating CM and FM optical depths was a reasonable compromise. The AHSRL
236 profile details as well as the corresponding derived values of τ_c^l , τ_c^o , τ_c^p , and the OPAL minus PEARL difference ($\Delta\tau_c$) are
237 shown in Figures S1a to S7a¹⁶ while the summary (profile- and event-integrated) VDR statistics for those lidar profiles are
238 given in Figures S1b to S7b of the same file (with the overarching VDR statistics being given in the table of Fig. S8). A brief
239 overview of those overarching statistics is given in Section A3.2.

240 Figure 2 shows the calculated cloud-screened CM AOD ~~values~~ during the apparent dust event of July 23, 2007 (~~what we call~~
241 ~~Event 5~~). We chose it to illustrate the key elements in support of our dust plume detection claims. The τ_c^l and $\tau_{c,1.5}^o$ values show
242 the high frequency variations that ~~we argue~~ are ~~arguably~~-due to near surface dust. The (high frequency) similarities between

¹⁴ over the extended period that the ~~three-two~~ data sets were ~~mutually~~ available (August 2005 to June 2010)

¹⁵ Appendix A3.1 is a discussion of how we filtered (weighted) out severe outliers that could appear in the VDR profiles

¹⁶ Supplementary PowerPoint file "AHSRL_CIMEL_event_profiles"

243 the τ_c^l and $\tau_{c,1.5}^o$ “spikes” (coupled with the low frequency unresponsiveness of $\tau_{c,1.5}^o$ to those spikes) are coherent with an
 244 argument for the presence of a weak, low-altitude dust event. The standard deviation (std) of $\tau_{c,1.5}^o$ is generally significantly larger
 245 than the std of $\tau_{c,1.5}^p$ (this disparity amounts to a quantitative verification of the relative unresponsiveness of $\tau_{c,1.5}^o$).
 246 The τ_c^l vs $\tau_{c,1.5}^o$ statistics show marginal to moderately large correlation coefficients (R values from 0.41 to 0.64) for each one
 247 of the seven events (the intra-event statistics) while the inter-event correlation coefficient for the ensemble of seven events
 248 was significant (R = 0.78). The τ_c^l vs $\tau_{c,1.5}^o$ intra-event statistics show marginal to moderately large correlation coefficients (R
 249 values from 0.41 to 0.64) for each of the seven events while the inter-event correlation coefficient for the ensemble of seven
 250 events was significant (R = 0.78).
 251 —The complete ensemble of individual CM AOD measurements in August and July 2007 show diurnal examples of what we
 252 determined to be largely dust-free conditions in the OOPAL to PEARL layer. A particular example on July 19, 2007, occurred
 253 in the presence of very clear background columnar conditions above the OOPAL and PEARL CIMELs¹⁷; it was thus an explicit
 254 example of clean background conditions that could be used as reference for declarations of time-varying dust events in the
 255 layer between the two events.
 256
 257

Formatted: Font: Not Bold, Complex Script Font: Bold

Formatted: Font: Not Bold, Complex Script Font: Bold

Formatted: Font: Not Bold, Complex Script Font: Bold

Formatted: Font: Not Bold, Complex Script Font: Bold

Formatted: Font: Not Bold, Complex Script Font: Bold

Formatted: Font: Not Bold, Complex Script Font: Bold

Formatted: Justified, Indent: Before: 0 cm

¹⁷ Across that layer we found $\Delta\tau_c^l$ and $\Delta\tau_c^o$ to be quite small ($\ll 0.0003$) and $\ll 0.0002$ respectively).

Formatted: Font: 9 pt, Complex Script Font: 9 pt

Formatted: Font: 9 pt, Complex Script Font: 9 pt

Formatted: Font: 9 pt, Complex Script Font: 9 pt

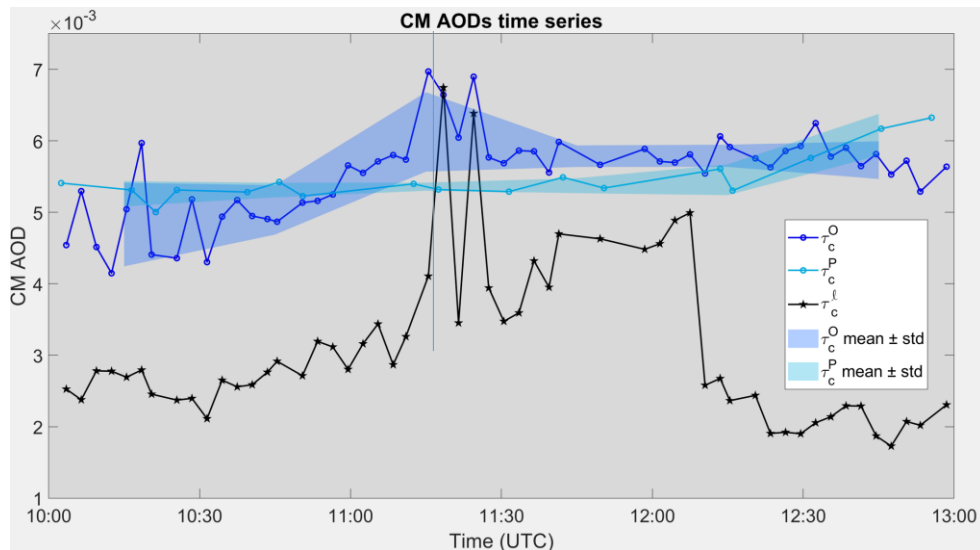


Figure 2 – Level 1.5 (cloud-screened) CM AOD time series of the July 23, 2007, dust event (Event 5 of our 7 dust events) for the CIMELs at 0PAL ($\tau_{c,1.5}^O$) and PEARL ($\tau_{c,1.5}^P$) as well as the 0PAL AHSRL (τ_c^f) (altitude range of 5 to 615 m). The δ_{thr} value for separating CM and FM AODs was 5%. $\tau_{c,1.5}^O$ should, normally, be greater than $\tau_{c,1.5}^P$ but the nominal CIMEL accuracy of ~ 0.01 / airmass (for both the 0PAL and PEARL CIMELs) is a key factor in the absolute comparison of these very small CM AOD values. The solid, blue-toned bands show the running standard deviation (std) about the running mean over 30-minute intervals with the first-interval mid-point starting at 10:15 UTC¹⁸. ~~The standard deviation of the former over the latter is significantly larger except near the end of the event (this disparity amounts to a quantitative check on the relative unresponsiveness of $\tau_{c,1.5}^P$)~~

4.1.2 Optical vs microphysical (ground-based) analysis at Eureka

Figure 3 encapsulates the analysis that we carried out in the comparison of the CIMEL CM AODs and APS v_c values associated with an event that we argue was a significant dust event at Eureka. The simultaneous rise of the APS v_c values and the $\tau_{c,1.5}^O$ time series after 20:30 UTC in Figures Fig. 3c and 3d are likely the start of a CM-aerosol event which this and other evidence (see Section 4.1.3) suggests was a dust event. The zoomed Fig. 3d shows a rather remarkable $\tau_{c,1.5}^O$ vs v_c correlation with

¹⁸ We produced these bands to focus on the high frequency differences between $\tau_{c,1.5}^O$ and $\tau_{c,1.5}^P$ (to avoid the standard deviation contributions of more low frequency variations)

272 departures from that correlation in the neighbourhood of $\tau_{c,1.5}^0$ and v_c peaks at, respectively, ~ 21:30 and 00:30 UTC (the
273 former could be ascribed to very thin cirrus clouds that we failed to detect in any satellite data while the latter could be the
274 result of a very spatially-variable dust plume). During this particular event, two large temporal spikes were eliminated from
275 the Level 1.0 retrievals by the AERONET temporally-driven (Level 1.5) cloud-screening algorithm (~~because the Level 1.0~~
276 ~~AERONET product of “Coarse AOD” can include CM cloud particles as well as CM aerosols¹⁹~~). During this particular event,
277 two large temporal spikes were eliminated from the Level 1.0 retrievals by the AERONET temporally-driven (Level 1.5)
278 cloud-screening algorithm. Supporting data for this elimination²⁰ is presented in Figures S9 to S11 where we demonstrate that
279 the Level 1.0 CM AOD spikes represent cirrus clouds that temporarily fouled the CIMEL sun-pointing FOV as determined
280 using the MISR sensor.²¹

281 The inferred approximate position of a smaller-radius AERONET PVSD peak in Fig. 3a and the APS peak in Fig. 3b (the cyan
282 curves at 21:00 UTC) suggests a common mode peak ~ 1.3 – 1.5 μm (with the AERONET peaks at radii $\geq 6 \mu\text{m}$ being outside
283 the radius range of the APS). The 1.3 – 1.5 μm peak radius is ~ 1.3 μm AERONET inversion peak reported by SDN in their
284 analysis of local dust at the Kluane Lake²² AERONET station in the Canadian Yukon (while the 6 μm AERONET peak is near
285 the upper limit of the reported KLRS peak radius range from ~ 4 to 7 μm for the 5 largest CM AOD cases; see Fig. 9 of that
286 paper). However, the KLRS CM AODs were ~ 2 to 14 times the CM AODs of the event shown in Fig. 3c (after the onset of
287 the significant rise around 20:30 UTC for which the CM AODs are ~ 0.006 to 0.016 or a $\Delta(\text{CM AOD}) \sim 0.01$). In general, dust
288 plumes in the Lhù’ään Mân’ region (associated with drainage basins of significantly greater relief than the region of Eureka)
289 demonstrated a CM AOD domination relative to the dust plumes that we claim to have found at OPAL (Fig. 3c).

290 SDN speculated that the smaller CM (1.3 μm) AERONET-inversion peak was more likely ascribable to springtime Asian dust
291 (while noting that the PVSDs measured with the TSI Optical Particle Sizer (OPS) device at KLRS showed no distinguishable
292 peak that was comparable with the 1.3 μm AERONET-inversion peak²³). However, the results presented in Fig. 3b suggest a
293 ~ 1.4 μm (small CM) APS peak that is clearly not due to springtime Asian dust (and thus could be ascribable to

Commented [NO2]: Deleted in deference to Reviewer 2 (this is information that is not essential to the paper)

Commented [NO3]: Again deleted in deference to Reviewer 2 (and again, not information that is essential to this paper)

¹⁹ ~~We would point out that this is not the case for FM particles: the AERONET FM AOD product amounts to a separation of FM aerosols from CM aerosols because cloud particles do not populate this particle size range.~~

²⁰ beyond the support provided in the AERONET literature for the efficacy of their cloud screening algorithm

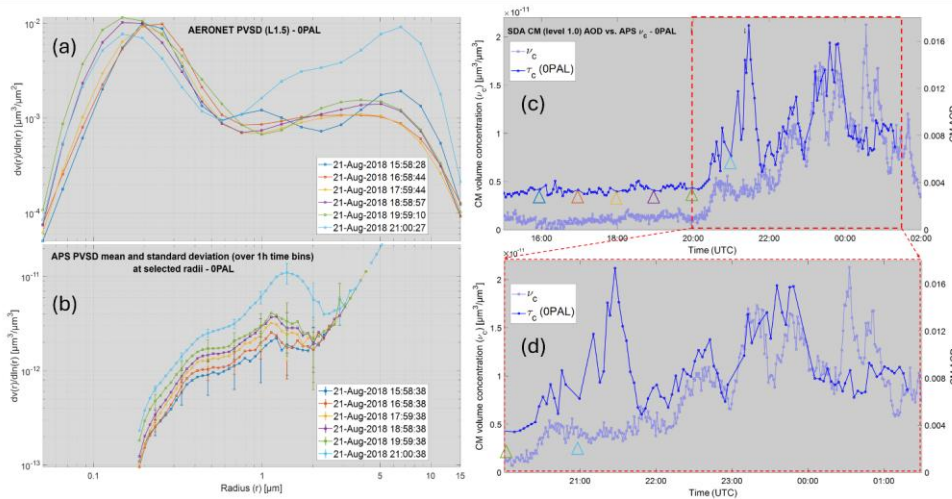
²¹ The MISR multi-angle (stereoscopic) capabilities permitted an estimate of the time that the roughly 8 km altitude cirrus cloud (located over Axel Heiberg Island) incited a spike in the Level 1.0 CM AOD.

²² This is the name AERONET ascribed to the CIMEL of the Lhù’ään Mân’ region. SDN referred to the AERONET CIMEL measurements being made at KLRS (Kluane Lake Research Station): ~~this KLRS is the place-acronym name that~~ we will associate with the “Kluane Lake” CIMEL

²³ ~~While two “Down Valley” OPCs (closer to or even a part of the source region and about 7 km west of KLRS) showed robust peaks ~ 1.7 μm :~~

phenomenologically different dust PVSDs and CM AODs than those of the much more dynamic and optically strong KLRS site). We believe that (i) the levels of PVSD-shape correspondence found between the AERONET and APS PVSDs as well as the higher-frequency temporal correspondence between the AERONET CM AOD values and the APS v_c values and (ii) the purely optical low-level plume evidence presented above for the July 23, 2007 case (the correspondence between τ_{cA}^{PO} and τ_c^l), lend credence to a claim of having measured, two independent low-level and optically weak (local) dust events at the Eureka OPAL site (the CIMEL Δ (CM AOD) increases during both events were respectively $0.007 - 0.004 = 0.003$ and $0.016 - 0.006 = 0.010$). The detection of such optically weak events (which effectively amount to lower limits of precision in ground-based dust AOD detectability) help to inform (appreciate certain limitations of) any satellite-based (CM AOD) search for optically detectable local dust events across the CAA. In the first instance, such weak events would seem to be detectable from a satellite sensor such as MODIS whose nominal precision appears to be significantly smaller²⁴. However, MODIS AOD precision is clearly an excessively optimistic (out of context) statement since that (coarse numeric scale) precision estimate in the presence of very small AODs would, no doubt, dramatically change (not to mention the fact that the nominal accuracy of the 3 km MODIS product (± 0.04) is much larger than the nominal precision).

Formatted: Not Highlight



308

²⁴ A nominal precision of $0.04 \times \Delta AOD$ which for our 2018 CM AOD range yields $0.04 \times 0.01 = 0.0004$ (i.e. $0.04 \times \Delta AOD$ for the best precision case of the 3 km DT over the open-ocean AOD product; Remer et al., 2013).

309 Figure 3 – (a) AERONET inversion PVSDs for the claimed dust event of August 21, 2018, (b) APS hourly-averaged PVSDs at the
310 times of the AERONET PVSDs (with standard deviations shown as error bars). Note that the APS points beyond $\sim 3 \mu\text{m}$ radius
311 were either superimposed and/or free of counts in a given bin (c) SDA Level 1.5 CM AOD ($\tau_{c,1.5}^0$) and APS v_c time series and (d)
312 ~~Zoom a zoom~~ of (c) ~~to at~~ the claimed time of the dust event. The triangles shown in (c) indicate the approximate time of the
313 AERONET and APS PVSDs (color coded to match the colors of the 6 PVSD cases in (a) and (b))²⁵. ~~The original high-frequency 3D~~
314 ~~(1 minute sample frequency) time series of APS PSDs are available upon request from the authors.~~

315 4.1.3 Satellite imagery versus ground-based measurements at Eureka

316 The synchronicity between the CM APS v_c and the $\tau_{c,1.5}^0$ time series on August 21, 2018 (after 20:30 UTC) coupled with
317 evidence of what were likely dust plumes over Eureka Sound (notably weak, grey-white plumes that appear to stretch across
318 Eureka Sound²⁶ at and south of the entrance of Slidre Fjord) provide regional evidence for the possibility of a very weak dust
319 event at OPAL (that was probably incited by the strong (generally north to south) winds of Figure S12 as they travelled over
320 the Fosheim Peninsula landmass north of OPAL). While Sentinel-2 clearly sees apparent dust plumes in Eureka sound (that
321 MODIS AOD imagery suggests is $\lesssim 0.03$ ²⁷) even the Sentinel-2 imagery, would likely not detect a sub 0.01 CM AOD (the
322 post 20:30 UTC $\tau_{c,1.5}^0$ OPAL CM AOD values of Figures 3c and 3d): the explicit image evidence for weak plumes over or near
323 the OPAL site is ambiguous at best.

324 Figure 4 shows the temporal variation of the Eureka wind speed (ws) and wind direction for Aug. 21 and 22. The rapid increase
325 at $\sim 21:00$ UTC in the v_c and $\tau_{c,1.5}^0$ time series of Fig. 3c is within the period of significantly high-amplitude ws values from
326 18:00 Aug. 21 to 18:00 Aug. 22 (the red-filled points of Fig. 4). This behavior is broadly consistent with CARRA (Copernicus
327 Arctic Regional Reanalysis) near-surface simulations in the neighbourhood of Eureka Sound to the west of OPAL (the region
328 of the Aug. 21 dust plumes in the Sentinel-2 image of Fig. S12). We would argue, based on the CARRA spatio-temporal
329 simulations of generally weaker ws values at 18:00 UTC to generally stronger values at 21:00 UTC over the Eureka Sound /
330 OPAL region²⁸, that a significantly strong regional wind event²⁹ incited the Eureka Sound Aug. 21 dust plumes and the attendant
331 v_c and $\tau_{c,1.5}^0$ increases near OPAL (the latter plumes likely being induced by northerly winds traversing the slopes of the
332 Fosheim Peninsula).

²⁵ ~~Note that the original high-frequency 3D (1-minute sample frequency) time series of APS PSDs are available upon request to the authors.~~

²⁶ See Figures S12 and S13 in the supplementary PowerPoint file “Satellite_Analysis”. The high spatial resolution (10 m pixels) of the Sentinel-S2A image and the overlain wind-vector field of Fig. S12 along with the blinking Sentinel-S2A images of 19:49 and 20:40 UTC acquisition times, suggest that dust plumes in Eureka Sound likely originated from the barren western slopes of Axel Heiberg Island.

²⁷ Very spatially coarse AOD pixels of 3 km resolution: Eureka Sound is $\lesssim 3$ MODIS-AOD pixels in width

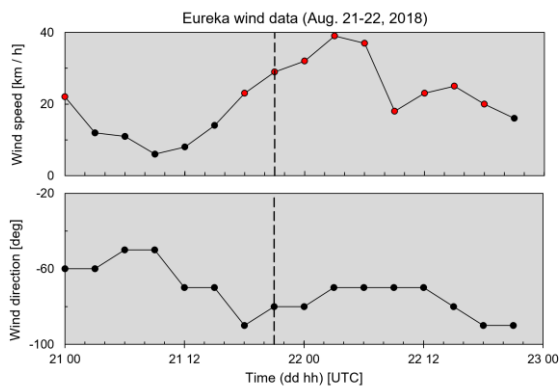
²⁸ as per Figures S32g and S32h of the Supplementary PowerPoint file “CARRA_wind_simulations”

²⁹ Roughly (qualitatively) lasting from 18:00 Aug. 21 (Fig. 32g) to 06:00 Aug. 23 (Fig. 32s).

Commented [NO4]: Made this comment a part of the figure caption to reduce the number of footnotes a bit (again, in deference to referee 2)

Formatted: Font: Bold, Complex Script Font: Bold

Formatted: Font: Bold, Complex Script Font: Bold



334

335 **Figure 4 – Temporal variation of the wind speed and wind direction for Aug. 21 and 22, 2018 (data from the ECCC “Eureka Climate”**
 336 **station very near 0PAL). The wind direction is defined as the direction that the wind is coming from relative to the station meridian.**
 337 **Positive and negative wind directions refer to CW and CCW angular departures from the meridian. The red-filled points indicate**
 338 **wind speeds that are above the mean + standard deviation ($15.5 + 2.5 = 18$ km / h) value of the Eureka (August) windspeed**
 339 **climatology reported in Fig. 5 of Lesins et al. (2010). The dashed vertical line shows a time (21:00 UTC) that is representative of the**
 340 **significant rise in CM AOD ($\tau_{c,1.5}^0$) and APS v_c values in Fig. 3.**

341 **4.2 Satellite-based RS of local dust events across the CAA**

342 We ~~also~~ employed satellite-based RS to investigate potential dust events over CAA sites where there was no ground-based
 343 sensors. Our goal here was to gain more ~~general~~ insight into satellite-based RS capabilities in different types of Arctic
 344 environments. A strong motivation for the CAA analysis was our belief that satellite-based dust RS findings over a variety of
 345 CAA sites would help build confidence in the satellite-based RS of dust events in general and weaker dust events in particular.
 346 Each one of our dust event cases below includes a small CAA map with the position of the event indicated by a green star.

347 **4.2.1 Large-scale dust event in the northern part of the CAA**

348 Figure 5a shows an Aqua true color image³⁰ of a dust plume that appears to originate from Axel Heiberg Island³¹ and flow
 349 along the open water of Eureka Sound and Greely Fjord. The thumbnail images of Figures 5b and 5c show respectively, the

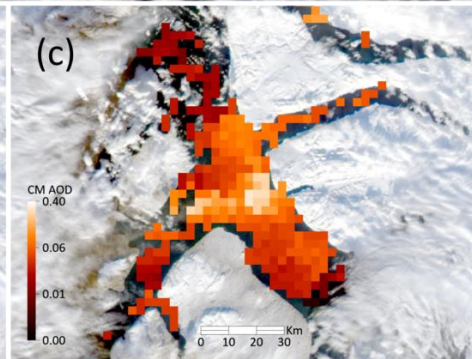
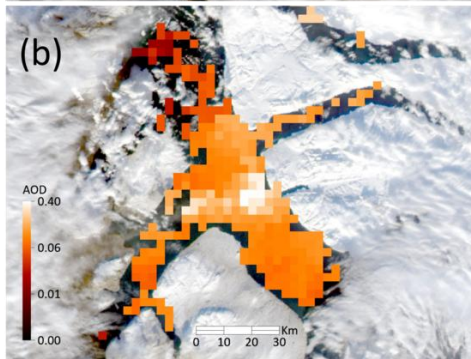
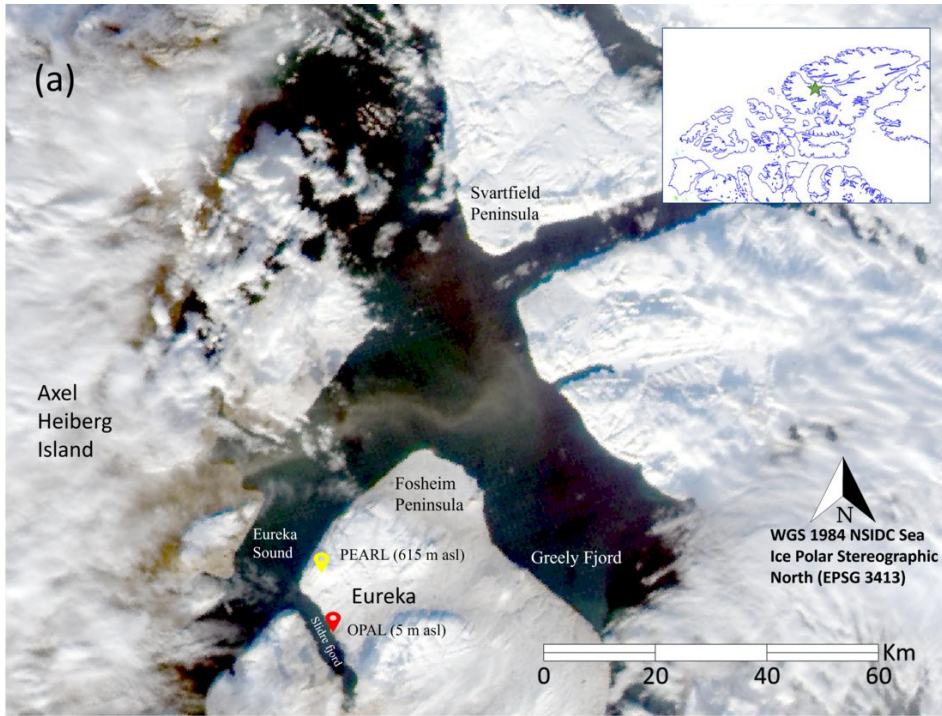
³⁰ Acquired at 15:20 UTC (late morning local time) on September 8, 2020

³¹ it appears to be emanating from the largely barren drainage basin whose watershed empties into Eureka Sound (see Fig. S15 for details).

350 MODIS-Aqua AOD and CM AODs (3 km resolution product) superimposed on the color image. Figure S14a³² shows a zoom
351 of the Aqua color image blinking with the AOD and CM AOD products alongside a map of the region (we recommend looking
352 at such zooms for details). The plume is most evident as it crosses Greely Fjord along its northeastward path and then appears
353 to veer northwestward towards the coast of the Svartfjeld Peninsula. This flow pattern is generally supported by the surface
354 *ws* vector field of Fig. S14b (including a final CCW turning (backing) in Greely Fjord followed by a CW turn (veering) of the
355 dust plume towards Svartfjeld Peninsula³³). The CM AOD values of Fig. S14a show a spatial pattern that includes a band of
356 moderately stronger CM AOD values which are coherent with the northeast-flowing spatial pattern of greyish intensity
357 variations in the true-color image (less evident but still notable is the CM AOD and greyish-intensity pattern matching of the
358 weaker plume that has veered in the northwesterly direction). The CM AOD values vary from extremes of ~ 0.02 to 0.31 (AOD
359 extremes of 0.06 to 0.42).
360

³² Supplementary PowerPoint file "Satellite_Analysis"

³³ There are no MINX (MISR) plume height or speed retrievals to report because the plume was basically obscured by clouds at the MISR orbit time of 19:50 UTC.



362 **Figure 5 – (a) MODIS Aqua true color image acquired at 15:20 UTC on Sept. 8, 2020, (b) and (c) MODIS Aqua AOD product and**
363 **derived CM AOD products respectively (superimposed on the true color image: see Fig. S14a for a detailed (zoomed) overlain**
364 **comparison of (a), (b), and (c)). See Section 3.4.1 above for the expression relating CM AOD to AOD.**

365 4.2.2 Dust event in the central southern part of the CAA

366 Figure 6a shows a (Sept. 26, 2015) MODIS-Terra, true color image of local dust plumes apparently emanating from Prince of
367 Wales Island (in the central southern part of the CAA) and moving in a northwesterly direction towards Victoria Island (image
368 acquired at 19:10 UTC). The true color image, along with the MODIS AOD products of Figures 6b and 6c, supported by the
369 MISR stereoscopic multi-look animation (see Fig. S16³⁴ and its caption for details) reaffirm the presence of dust plumes
370 flowing in a northwesterly direction. The color image and MODIS AOD products of Fig. 6 (see Fig. S17 for greater detail)
371 support a claim of distinct individual dust plumes. The CM AOD and AOD values of the plumes (whose spatial variation is
372 visually coherent with the variations of the plume-like structure seen in the color image) vary respectively, across extremes of
373 0.02 to 0.56 and 0.06 to 0.73). The [high-resolution Google Earth](#) landcover map (Fig. S18) shows a 20-km wide barren region
374 which appears to be the dominating influence as the source of the dust plumes (judging by the color image combined with the
375 MODIS AOD product).

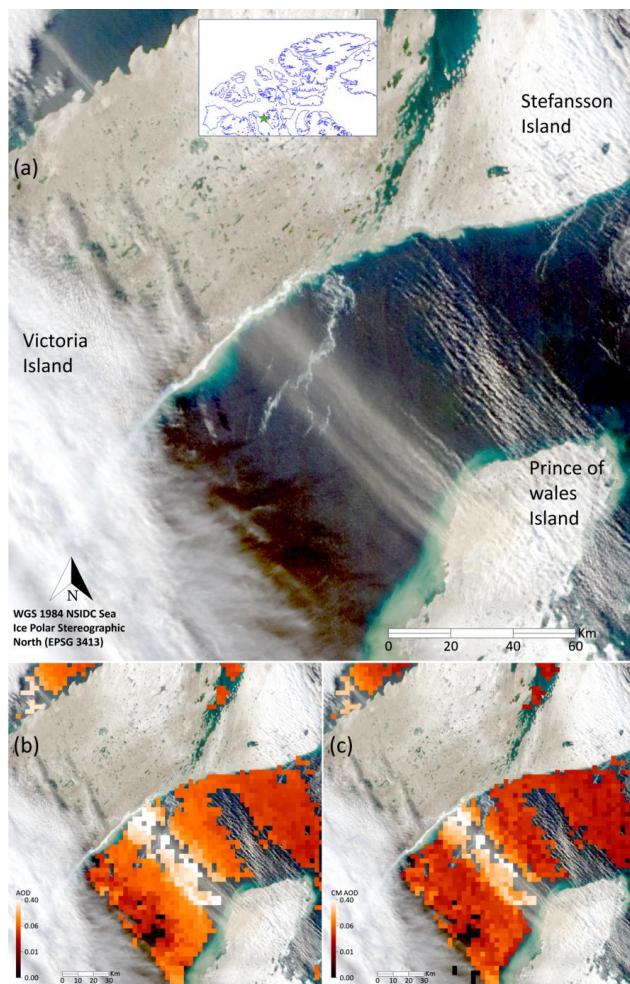
376 A sampled MISR trajectory in the direction of the dust plume (the orange-colored trajectory on the MISR color image of Fig.
377 7a) shows wind-corrected plume height along that trajectory while Figures 7b and 7c show, respectively, plume heights as
378 a function of trajectory-sample number and the plume heights histogram. The analogous pair of trajectory and histogram graphs
379 for plume speed are shown in Figures 7d and 7e. The average MINX (MISR) plume height \pm its standard deviation is $298 \pm$
380 230 m ASL³⁵. The mean and standard deviation of the MISR wind (plume) speed histogram ($\langle ws \rangle \pm \sigma(ws) = 75 \pm 24$ km
381 / h or 54 ± 17 km / h when normalized to near surface conditions³⁶). This $\langle ws \rangle$ value is \sim the 19:00 UTC Sept. 26, 2015
382 Stefansson Island met station ws value of 49 km / h and \sim 3-times the (2002 – 2024) Stefansson Island climatological mean
383 for the month of September (17.7 ± 10.9 km / h).

384

³⁴ Supplementary PowerPoint file “Satellite_Analysis”

³⁵ We note that in general, neither the plume height or the plume speed sampling trajectories are subject to any objective sampling protocol and that the plume height (and plume speed) histograms generally represent significant departures from a normal distribution. While we report means and standard deviations of plume height and wind speed, they are meant to be order-of-magnitude height and height variability indicators for subjectively selected plume structures seen in the color imagery.

³⁶ An ECCC met station (WMO ID: 71017, coordinates 73°46'N, 105°18') at 11 m elevation is located on Stefansson Island (see Fig. 6). We normalized the MISR plume speed to the plume speed at the elevation of the station by applying a standard wind gradient expression (see .e.g. Kaltschmitt et al., 2007) with an open-water wind shear (Hellman) exponent of 0.1: $ws(h) = ws_{ref}(h/h_{ref})^{\alpha}$, $ws_{ref} = ws(h)(h/h_{ref})^{-\alpha} = 75(298/11)^{-0.1} = 54$



385

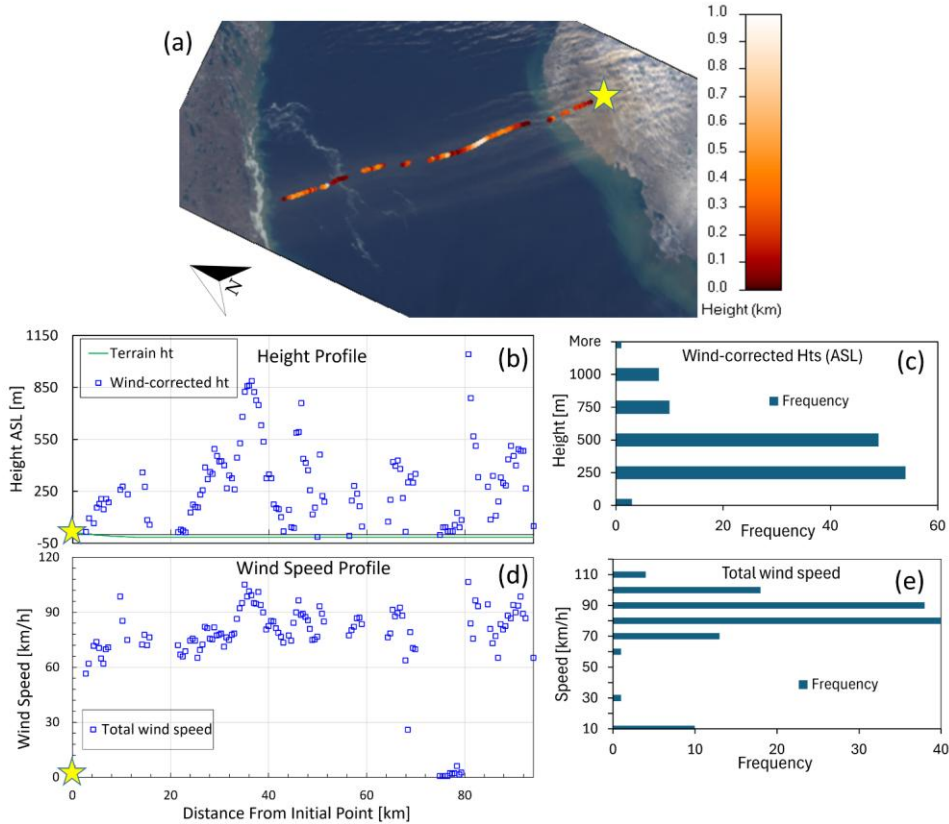
386

387

388

389

Figure 6 – local dust event (over Prince of Wales Island and Victoria Island) captured on 26 September 2015. (a) MODIS Terra true-color image acquired at 19:10 UTC (b) AOD product, (c) CM AOD. Note that there appear to be distinct water plumes before and after the barren region on Prince of Wales Island (water plumes that were captured by the MODIS cloud OD product and are distinctly unique in the color image).



391

392

393

394

395

396

397

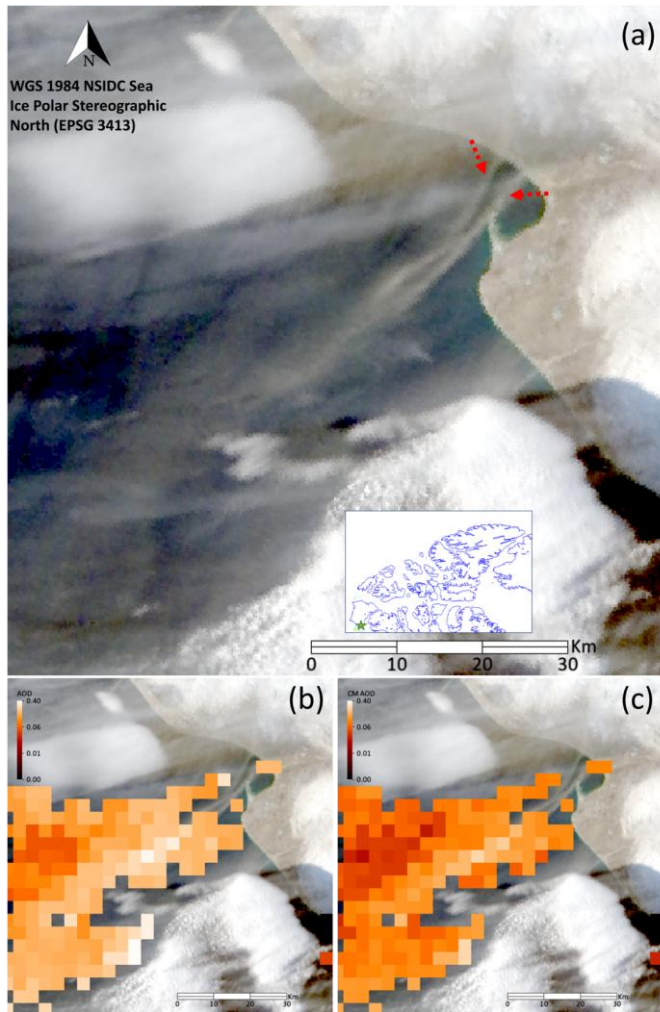
Figure 7 – (a) MISR nadir (An camera) true color image acquired at 19:12 UTC (275 m resolution) with retrieved MISR plume height values along a selected trajectory (the red-orange path that begins with a yellow star and whose color legend appears to the right of the image) superimposed on the color image, (b) trajectory plume heights as a function of distance from the reference point (yellow star) and (c) the histogram of those selected plume heights. The (d) and (e) graphs are the corresponding wind (plume) speed trajectory values and histogram. We note that the MINX assumption of no vertical plume motion may reduce the plume height retrieval accuracy (Nelson et al., 2013).

398 4.2.3 Dust event in the southwest corner of the CAA

399 The red arrows of Fig. 8a delineate what we argue are a pair of local dust plumes emanating from largely vegetation-free areas
400 on Banks Island (the southwest corner of the CAA) and flowing south over the Amundsen Gulf (MODIS-Terra color image
401 acquired at 20:20 UTC on October 1, 2018). Some plume widths are sufficiently thin that the moderate resolution MODIS and
402 MISR color imagery (as well as the coarser resolution of the MODIS 3 km AOD product) diffuses out much of the fine spatial
403 detail. The AOD product and the derived CM AOD (Figures 8b and 8c) appear to capture the general individual plume patterns
404 seen in the color imagery (and their apparent broadening into a single plume). The MODIS CM AOD values in the vicinity of
405 those plumes range from ~ 0.03 to 0.26 (while AOD values range from ~ 0.04 to 0.37).

406 This was a complicated case with high altitude cirrus being (at least qualitatively) confused with the very low altitude dust
407 plumes. The issue can, on a visual level, be resolved by deferring to animations of the multi-angle MISR views where the
408 separation of the former from the latter (in terms of their apparent stereoscopic ground speed relative to the fixed ground scene)
409 is evident (see that animation in Fig. S19). Figure S20 shows a sampling trajectory of the double dust plumes that are pointed
410 to by the red arrows of Fig. 8a. The mean and standard deviation of the MISR plume height and wind (plume) speed histograms
411 along this trajectory are respectively 196 ± 155 and 25 ± 25 km / h (the latter value belonging to a distinctly non-normal
412 distribution).

413 The geographic details of the two thin dust plumes seen in the MODIS-Terra color image of Fig. 8a along with even weaker
414 and thinner dust plumes elsewhere in the region are brought into rather striking relief in zooms of a high-resolution Sentinel-
415 2 image. Figure S21 shows, what amounts to, apparent source information for five different plumes (including source
416 information for one of the two thin dust plumes seen in the MODIS image). Those zoomed images give valuable, if indirect,
417 contextual information on the source and dynamics of the plumes. One can, for all five cases, see a water to land dust plume
418 continuity with the plume origins being either (a) very low altitude dust plumes over the land or (b) surface features of the
419 sources.



420
 421 **Figure 8 – (a) Local dust plumes emanating from Banks Island on October 1, 2018 (MODIS Terra true color image acquired at**
 422 **20:20 UTC). Figures (b) and (c) show the MODIS Terra AOD and the derived CM AOD superimposed on the color image**

423 4.3.4 Dust plumes emanating from Ellef Ringnes Island (eastern part of the central CAA)

424 The 20:10 UTC, September 13, 2014 MODIS-Terra true color image of Fig. 9a shows what appear to be local dust plumes
425 emanating from dark brown regions of Meteorologist Peninsula³⁷ and flowing over the open-water region at the southern tip
426 of that peninsula. Figures 9b and 9c show the MODIS AOD product and estimated CM AODs over a part of that open-water
427 region: the spatial variation of those AODs and CM AODs are qualitatively coherent with the perceived spatial variations of
428 the dust plumes in the true color image of Fig. 9a. Figure S23 shows zoomed-in details: one can observe that the thickest part
429 of the plumes as seen on the color image and the largest CM AODs are aligned with the brownish regions (presumably sources)
430 on Meteorologist Peninsula. CM AOD values in Fig. 8b and 8c range from ~ 0.05 to 0.47 while the AOD values range from ~
431 0.11 to 0.50.

432 Figures S24 and S25 show a selected MISR trajectory case over the open water west of Meteorologist Peninsula (Fig. S22
433 shows the [subjective] investigation that was carried out to determine the color image enhancement that best permitted one to
434 appreciate how the trajectory was embedded in the dust plume³⁸). The mean wind-corrected plume height is 264 ± 162 m for
435 the trajectory while the mean plume speed is 38 ± 14 km / h. Normalizing the latter value to the height of the nearest met
436 station³⁹ yields normalized wind speeds of 32 km / h. This is moderately lower than the 20:20 AUT ~~measured-met station~~ value
437 of 51 km / h and 1.7-times its climatologically (1996 – 2025) mean wind speed for the month of September (18.8 ± 13.5 km /
438 h).

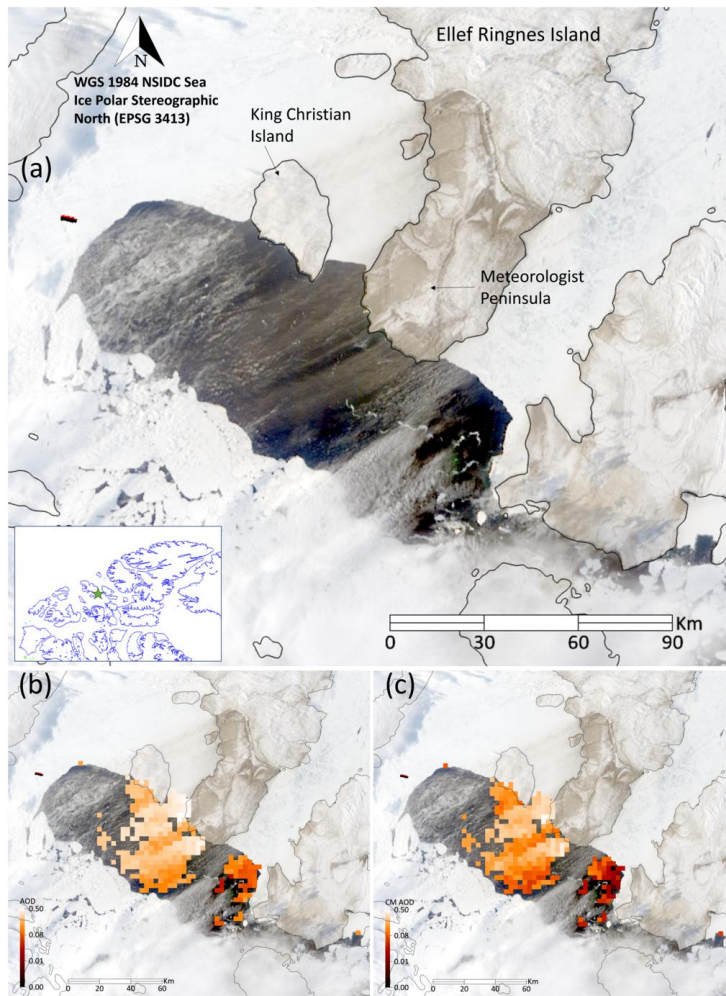
439 In the absence of a standard AOD product we developed an ad hoc AOD retrieval technique for the dirty brown snow/ice
440 region between Meteorologist Peninsula and King Christian Island (see Fig. S26 and its caption for details on that ad hoc
441 technique). The results of that retrieval showed a coarse degree of AOD continuity across the ice/snow to water interface⁴⁰
442 (see the blinking animation of Fig. S27). Evidence that the dirty brown area was (at least in part) a dust plume and not deposited
443 dust is provided by a MISR height profile showing plume heights varying between 0 to ~ 500 m (Fig. S28). The corresponding
444 plume speeds of 42 ± 20 km / h are moderately greater than the plume speeds over water.

³⁷ Meteorologist Peninsula is located at the extreme south of Ellef Ringnes Island (again, see Fig. 9a)

³⁸ Figure S24 shows the MISR camera animation where one can more readily appreciate the positions and stereoscope movement of higher altitude clouds.

³⁹ The 58 m ECCC met station of “ISACHSEN (AUT)” in the north of Ellef Ringnes Island (78°47’N, 103°33’W). The normalization approximation for wind-shear (wind gradient) effects was carried out as per Section 4.2.2 above.

⁴⁰ there is no CM AOD option for the snow/ice retrievals since we have no CMF estimate for those retrievals



445

446

447

448

449

Figure 9 – MODIS-Terra true color imagery (logarithmic enhancement) acquired at 20:10 UTC over Ellef Ringnes Island on Sept. 13, 2014 (a) local dust plumes over the water emanating from Meteorologist Peninsula on Ellef Ringnes Island. Figures (b) and (c) show the MODIS Terra AOD and derived CM AOD superimposed on the color image (see Fig. S23 in the supplementary PowerPoint file “Satellite_Analysis” for a full resolution comparison of the AODs and the color image).

4.4 Surface plume deposition / snow melt; snow/ice reflectance changes as optical precursors of dust plumes

The RS of airborne Arctic dust can be advantageously complemented by the RS of reflectance changes (darkening) induced by the deposition of airborne dust on snow or ice and/or reduced reflectance incited by premature snow melt due to dust deposition. Woo et al. (1991) noted that the presence of snow-melt zones over the Fosheim Peninsula on Ellesmere Island corresponded to dark spots in early AVHRR imagery. Ranjbar et al. (2021) found roughly the same dark patterns in true color MODIS imagery and showed visual evidence of deposition of dust on snow (or ~~the snow-melt product of~~ underlying soil ~~subsequent to snow melt~~) in a mosaic of true color MODIS imagery acquired over the whole of Ellesmere Island. O'Neill et al. (2025) argued that the combination of persistent day to day dark zones in MODIS imagery and the lack of movement of those features in MISR multi-angle imagery was indicative of local-dust surface deposition in the case of Prince Patrick Island and neighbouring Eglinton Island (west central CAA). We found what appeared to be a more dynamic MISR example of deposited dust across the Strand Bay region of Axel Heiberg Island over a three-day period (see Fig. S29). Figure S30a shows the MISR height profile of a June 8, 2007, airborne dust plume and the position of its sampling trajectory on the associated MISR (nadir) image⁴¹. The plume profile of Fig. S30b (acquired two days later) shows what appears to be near-zero heights in a region where the color image indicates a much darker pattern than that of Fig. S30a⁴² (accompanied by a rise in plume height near the northern shore of Strand Bay). We would suggest that the darkest region of Strand Bay in the color image is likely a dynamic example of the process of dust deposition. In this particular case, the source of the (very dark) dust is likely the volcanic deposits known to characterize much of the Strand Fjord Formation (Williamson & MacRae, 2015).

5 Conclusions

Ground-based RS and microphysical measurements acquired at the PEARL complex in Eureka were employed to investigate the potential for satellite-based and ground-based RS of local dust plumes. This analysis ~~was~~ supported and / or complemented ~~by~~ explicit examples of satellite-based RS of local dust events near Eureka and across the CAA.

Ground-based RS validation results were obtained (in terms of the identification and characterization of local dust events) with significant correlations ~~in 2007 data~~ between the OPAL (ground-based) CM AOD and the lidar-derived CM AOD (and the lack of correlation with the 615 m above-plume CM AOD at the Ridge Lab). ~~The late-summer correlations (Aug. 21, 2018 data) between APS CM particle-volume concentration (v_c) measurements and OPAL CM AODs along with the similarity between the APS and AERONET PVSDs suggest a significant 1.3 – 1.5 μm radius peak that was due to local dust of weak CM AOD (≤ 0.01). Comparisons between AERONET and APS PVSDs strongly suggested that both types of instruments were sensitive to local dust PVSD peaks – 1.3 – 1.5 μm radius. This was similar to~~ notable given the near-1.3 μm radius AERONET peaks reported by SDN for a springtime (May) measurement campaign at the KLRS site in the Yukon (a peak which they

Commented [N05]: I can't believe that we missed this duplication of sentences!

⁴¹ The MISR image shows numerous dust plumes which appear to be associated with dark sources on the southern shore of Strand Bay.

⁴² Note that the MISR times of S30a and S30b images are nearly identical (solar illumination conditions are nearly identical)

479 described as likely being associated with ascribed to springtime Asian dust). The correlations between APS-CM particle volume
480 concentration (v_p) measurements and OPAL-CM AODs along with the similarity between the APS and AERONET PVSDs
481 suggest a significant 1.3–1.5 μm radius peak that was due to local dust of weak CM AOD ($\lesssim 0.01$).

482 Indirect linkages were made between the surface RS and microphysical data and available satellite on the Aug. 21, 2018, RS
483 imagery acquired in the neighbourhood of Eureka: we argued that a weak but detectable plume over Eureka Sound (MODIS
484 AODs $\lesssim 0.1$) might be related to the very weak CM AODs measured by the OPAL CIMEL (values of $\lesssim 0.01$ that are typically
485 undetectable by satellite RS). More direct linkages were made with OPAL wind speed (ws) measurements and regional ws
486 (reanalysis) values. It was argued that above normal OPAL ws values and above normal regional ws values coupled with co-
487 incident increases in CM AOD and $v_c(0)$ measurements at OPAL were evidence of a region-wide wind event that caused local
488 and regional dust disturbances.

489 A pan-CAA analysis using the multi-dimensional information available from MODIS color imagery and its AOD products,
490 MISR multi-camera, stereoscopic imagery, MINX (MISR) estimates of plume height and speed and high spatial resolution
491 Sentinel-2 imagery supported by measured and /or regional ws products indicated that local dust plumes of relatively weak to
492 strong optical thickness (CM AOD ranging from ~ 0.02 to 0.60) at generally sub-km plume heights could be detected from
493 available satellite products. A sampling of key parameters for all plume events is given in Table 1. In what follows we give a
494 summary of those pan-CAA conclusions.

495 A Sept. 20, 2020 plume event north of the Fosheim Peninsula showed evidence of plume dynamics that were roughly coherent
496 with CARRA wind vector patterns and whose spatial variation (colour image pattern) was similar to the spatial pattern of the
497 derived CM AODs. The MINX (MISR) plume height and speed of (September 26, 2015) dust plumes flowing from Prince of
498 Wales Island to Victoria Island (southern part of the CAA) were 300 ± 230 m ASL and 75 ± 24 km / h (while MODIS CM
499 AOD values ranged from 0.02 to 0.56). The 54 km / h value⁴³ for that event is abnormally large (3 times the climatological
500 mean for September).

501 Information from MISR, MODIS and Sentinel-2 color imagery was employed to identify dust plumes (partially obscured by
502 higher altitude clouds) emanating from local dust sources on Banks Island (southwest corner of the CAA) in October of 2018.
503 The MODIS CM AOD values, for the Banks Island satellite events varied from 0.03 to 0.26 and visually corresponded to
504 what appeared to be dust plumes in the MODIS color imagery (supported by the stereoscopically determined distinctions
505 between clouds and low-level plumes provided by the MISR imagery). The Sentinel-2 color imagery provided a unique high-
506 spatial-resolution perspective that enabled the distinction of the land to water continuity of a few local dust plumes. A
507 moderately strong dust event emanating from Ellef Ringnes Island in September of 2014 was characterized by CM AODs
508 between ~ 0.05 to 0.47, mean plume heights of $\lesssim 300$ m and mean plume speed (normalized to the elevation of the nearby met

⁴³ the measured value normalized to the height of the nearby met station

509 station) of 32 ± 12 km / h (1.7 times the climatological mean of the nearby [Stefansson Island] met station for the month of
 510 September).

511 ~~Finally, we~~ employed MINX (MISR) color imagery and plume height retrievals to argue that June, 2007 Strand Bay (Axel
 512 Heiberg Island) MISR images of a dirty snow / ice surface showed both a plume above the surface and what appeared to be
 513 plume deposition (zero altitude plume retrievals) over the surface two days later (with a much darker reflectance). This appears
 514 to be a rather rare ~~concrete~~ example of a commonly cited phenomenon (dust plume deposition effects). The RS identification
 515 of dust deposition events on snow presents a unique opportunity -for monitoring the attendant changes in snow reflectance
 516 (and premature snow melt events) across different Arctic regions.

517 In summary, a series of dust events involving distinct, narrow plumes, at least partly over dark water, downwind of likely dust
 518 sources and typically under contemporaneous high-wind conditions were identified. The use of the MODIS and/or MISR
 519 and/or Sentinel-2 imagery (coupled with geographical and meteorological information) for identifying and characterizing local
 520 dust plumes requires careful analysis: however, the benefits often include a synergistic characterization of plume properties
 521 that significantly exceed what can be extracted from a single sensor. The specialized advantages of each of these RS sensors
 522 should be understood before undertaking such an approach: our greatest strategic realization, for example, was that, in spite of
 523 the obvious advantages of the CALIOP lidar in characterizing dust plume properties, the MISR imager has a much greater
 524 chance of detecting a spatially constrained plume (CALIOP being limited to a single orbit line rather than broad, along-track,
 525 MISR images).

Commented [NO6]: The paragraph was missing a concluding consequence of being able to detect dust deposition events

526
 527 **Table 1: Summary of CAA dust events captured using satellite-based RS. See footnote 37 concerning the reporting of means and**
 528 **standard deviations for plume height and plume speed.**

Source location (Island)	Date and time (dd/mm/yyyy, hh:mm) [UTC]	Approximate coordinates of plume source (lat, lon) [deg]	AOD (min, max)	CM AOD (min, max)	Visible plume length [km]	plume height (ASL) [m]	plume speed [km/h]
Axel Heiberg Island	08/09/2020, 15:20	(80.05, -87.55)	(0.06, 0.42)	(0.02, 0.31)	60	NA	NA
Prince of Wales Island	26/09/2015, 19:10	(72.65, -102.36)	(0.06, 0.73)	(0.02, 0.56)	110	300 ± 230	75 ± 24
Banks Island	01/10/2018, 20:20	(71.46, -121.74)	(0.04, 0.37)	(0.03, 0.26)	50	196 ± 155	25 ± 25
Ellef Ringnes Island	13/09/2014, 20:10	(77.83, -99.50)	(0.11, 0.50)	(0.05, 0.47)	60	264 ± 162	38 ± 14
Axel Heiberg Island (Strand Bay)	08/06/2007, 19:59	(79, -93.25)	NA	NA	20	165 ± 99	1.6 ± 1.2
Axel Heiberg Island (Strand Bay)	10/06/2007, 19:47	(79, -93.25)	NA	NA	20	40 ± 40	2 ± 2

529

530 **Appendix A**

531 **A1: Comparing CIMEL- and AHSRL-derived AODs**

532 **A1.1: CIMEL-based FM and CM attribution**

533 Given the unique arrangement of the two ~~CIMELs~~ CIMELs at Eureka, one near the OPAL site (superscript “O” and one at
534 the higher altitude PEARL (Ridge lab) site (“P” subscript), the (500 nm) FM, CM and total AODs of the layer between the
535 two sites (assuming optical homogeneity above P between the two different lines of site) are,

536
$$\Delta\tau_f = \tau_f^O - \tau_f^P \quad (A1a)$$

537
$$\Delta\tau_c = \tau_c^O - \tau_c^P \quad (A1b)$$

538
$$\text{and } \Delta\tau_a = \tau_a^O - \tau_a^P = \tau_f^O + \tau_c^O - (\tau_f^P + \tau_c^P) = \Delta\tau_f + \Delta\tau_c \quad (A1c)$$

539 **A1.2: Temporal resampling considerations for the two CIMELs and the lidar**

- 540 1. $\tau_c^{l,O}$ represents τ_c^l resampled to τ_c^O times while we use $N^{l,O}$ to describe the number of resampled points. For the sake
541 of keeping the nomenclature as simple as possible, we dropped the “O” superscript from
542 $\tau_c^{l,O}$ (i. e. there is only one lidar).
543 2. $\tau_c^{p,O}$ represents τ_c^p resampled to τ_c^O times⁴⁴ while using $N^{p,O}$ to represent the number of resampled points. $N^{p,O} \neq$
544 $N^{l,O}$ if, for example, the PEARL measurements are limited in temporal extent relative to the OPAL temporal extent.
545 3. Accordingly, $\Delta\tau_c$ is more precisely defined as $\tau_c^O - \tau_c^{p,O}$.
546 We employ N^O to represent the common lidar and PEARL resample points ($N^O = N^{l,O} = N^{p,O}$).

547 The resampling applied to estimate τ_c^l or $\tau_c^{p,O}$ was respectively nearest neighbour⁴⁵ and linear interpolation⁴⁶

548 **A2: FM and CM attributions for the AHSRL lidar**

549 If the FM and CM PDR (particle depolarization ratio⁴⁷) candidates are defined by holistic FM and CM PDR distributions
550 (whose size-averaged PDRs are δ_f and δ_c) then the optically weighted average VDR can be written as:
551

⁴⁴ but τ_c^p is shown in the PowerPoint profiles

⁴⁵ the value of τ_c^l at the nominal τ_c^l time contained within a particular OPAL (one-minute) time bin (where the general
AERONET sampling frequency is every 3 minutes: see Giles et al., 2019 for details on CIMEL sampling),

⁴⁶ between the two τ_c^p values at the two nominal PEARL times on either side of a particular τ_c^O time

⁴⁷ A-PDR is a common (intensive-parameter) label for ~~of~~ that is typically (if rather simplistically) associated with a given type of atmospheric
particle. See, for example, Liu et al. (2013)

Formatted: Indent: Before: 0 cm

Formatted: Font: Italic, Complex Script Font: Italic

552
$$VDR = \frac{\delta_f \tau_{\beta,f} + \delta_c \tau_{\beta,c}}{\tau_{\beta,f} + \tau_{\beta,c}} \quad (A2a)^{48}$$

553
$$= \delta_f (1 - \eta_{\beta,c}) + \delta_c \eta_{\beta,c} \quad (A2b)$$

554
$$= \delta_f \eta_{\beta,f} + \delta_c (1 - \eta_{\beta,f}) \quad (A2c)$$

555 where we define

556
$$\eta_{\beta,c} = \frac{\tau_{\beta,c}}{\tau_{\beta,c} + \tau_{\beta,f}} \text{ and } \eta_{\beta,f} = \frac{\tau_{\beta,f}}{\tau_{\beta,c} + \tau_{\beta,f}} = (1 - \eta_{\beta,c}) \quad (A2d)$$

557 As we will argue below, the lidar optical depths (τ_c^l and τ_f^l in the main text⁴⁹) can provide reasonable estimates of τ_c and τ_f
 558 for a strategic choice of δ_{thr} . If the FM and CM PDRs are defined in a binary fashion by a δ_{thr} threshold then those PDRs
 559 can be written,

560
$$\delta_f' = \langle VDR^{\delta \leq \delta_{thr}} \rangle \quad (A3a)$$

561
$$\delta_c' = \langle VDR^{\delta > \delta_{thr}} \rangle \quad (A3b)$$

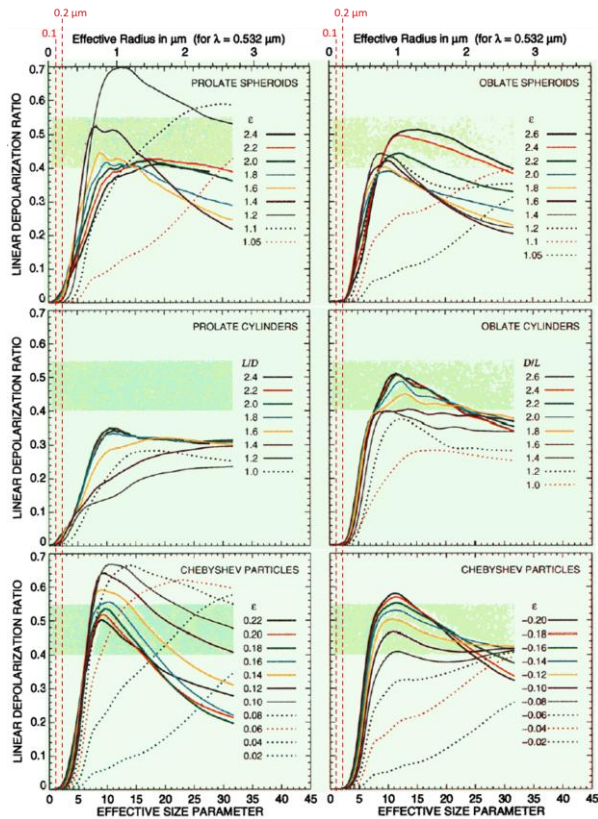
562 The “ $\langle VDR \rangle$ ” symbolism represents some weighted or unweighted VDR mean in altitude (or in altitude as well as time) where
 563 the δ_{thr} criterion is applied to every single lidar pixel. Equation (A2) represents a tool for seeking out information about the
 564 PDRs of holistic depictions of FM and CM components. One must be wary of the opto-physical differences between δ_f and
 565 δ_c versus δ_f' and δ_c' respectively⁵⁰ and their link with the measured VDR (or averages of measured VDRs). The two
 566 formulations can be investigated by varying δ_{thr} until some optimal solution is obtained for any given event. Part of the process
 567 is the recognition that δ_f is known (empirically and theoretically) to be small (\leq a few %; see Fig. A1 for example) while δ_c
 568 of dust particles generally increases with increasing δ_{thr} in the range where dust-particle population is significant⁵¹. We
 569 suppose that the PDR of other particulate species (clouds, for example) are easily separable from our FM and CM aerosol
 570 species.

⁴⁸ Where FM and CM (lidar profile) pixels can be defined, respectively by $\delta \leq \delta_{thr}$ & $\delta > \delta_{thr}$ if there is a δ_{thr} saddle between the PDRs

⁴⁹ where $\tau_c^l = S_c \tau_{\beta,c}$ and $\tau_f^l = S_f \tau_{\beta,f}$ (S_c and S_f being their respective lidar ratios)

⁵⁰ Equation (A2) represents a continuously varying function of η_c or η_f while equation A3 is a step function of δ_{thr} (stepping from δ_{thr} -
 dependent values of $\langle VDR \rangle$ for $\delta \leq \delta_{thr}$ to δ_{thr} -dependent values of $\langle VDR \rangle$ for $\delta > \delta_{thr}$)

⁵¹ Where the particle volume sized distribution is significant: see, e.g., Mamouri & Ansmann, 2014 (MA)



571
 572 **Figure A1** – Computed variation of the 532 nm DR as a function of effective radius (top horizontal scale) and various assumed ice
 573 particle shapes (Fig. 1 of Mischenko & Sasson, 1998). Optically significant, column-integrated FM particles are largely contained
 574 within a radius range of 0.1 to 0.2 μm (indicated by the red-dotted vertical lines which we appended to the original figure). This
 575 demonstrates that the PDR of FM particles is \lesssim a few % for all particle shapes considered by the authors.

576 **A3: The need for vertically-averaged VDR weighting**

577 AHSRL β and VDR profiles (along with derived values of lidar, OPAL and PEARL CM AODs) for the 7 Eureka dust events
 578 that we investigated can be observed in the supplementary PowerPoint file “AHSRL_CIMEL_event_profiles”. The VDR
 579 values ranged from small-amplitude negative to positive values to large-amplitude negative and positive outliers (see Section

580 A3.1 for a detailed discussion of how we processed that data). Dörnbrack et al. (2010) reported on airborne lidar observations
581 and characterization of local dust events over Svalbard in May of 2004. Their results included dust plumes whose VDRs ranged
582 from quite small ($\leq 5\%$) to values larger than 10% inside the plumes to maximum values of $\leq 30\%$ very close to the surface.
583 In the context of the discussion presented in Section A2, VDRs of local dust profiles can achieve (extreme FM to CM) values
584 $\sim 15 - 40\%$ ⁵². MA report that their holistic FM component⁵³ produces PDRs ($\sim 5\%$ ⁵⁴) while also demonstrating that their sub-
585 μm FM dust tail⁵⁵ can induce a significant VDR increase relative to the holistic FM component⁵⁶ and that super- μm particles
586 can induce even larger VDRs. See Figures 3a and 3b above for empirical examples showing a super- μm CM peak radius at
587 our OPAL site (after the advent of the stronger dust event at 20:30 UTC).

588 **A3.1: VDR weighting options.**

589 VDR profile averages ($\langle VDR \rangle$) between 82 and 615 m⁵⁷ were found, in the initial processing run, to be systematically too
590 large⁵⁸. This was suspected to be due to the initial choice of not including negative VDR pixels in any given VDR profile
591 average⁵⁹. Indeed, Fig A2 shows that the simple removal of negative VDR pixels (blue-colored circles) produced $\langle VDR \rangle$
592 estimates that were systematically greater than the two more statistically justifiable methods⁶⁰. Two alternate methods were
593 investigated to mitigate the impacts of removing negative VDRs :

- 594 ○ The 1st method (green circles) employs no weighting but does not exclude negative VDRs.

⁵² See, e.g. MA who argue that their FM and CM dust PDRs [$“\delta_{df}”$ and $“\delta_{dc}”$ respectively] of 16 and 39% respectively can generate near-source (Sahara) VDR (δ) values of $\sim 31 \pm 3\%$ (the values of Freudenthaler et al., 2009 and Grob et al., 2011 as cited in MA).

⁵³ e.g., the complete (and ubiquitous) FM AERONET-inversion component between $\sim 0.05 - 0.2 \mu\text{m}$ (radius) seen in their Fig. 4.

⁵⁴ for what they call “non-dust” particles but whose distinctive feature is arguably the limitation to a holistic FM component. See also, for example, the precipitous drop in simulated δ values of ice particles (to magnitudes $< 5\%$) for (ice) between the specific cases of 0.05 and 0.2 μm radius (effective size parameter between 0.6 and 2.4) in Fig. A1.

⁵⁵ the tail of what might be called a holistic CM component between ~ 0.2 to 10 μm radius as seen in their Fig. 4

⁵⁶ MA’s AERONET PSD shows a not insignificant (sub- μm) FM tail of that CM component. It is this tail that surely drives their FM ($“\delta_{df}”$) estimate of 16 %.

⁵⁷ the difference in elevation between OPAL and PEARL (except that the 82.5 m is above the OPAL elevation of 5 m). The statistics start at 82.5 m because the VDR below 82.5 m was judged to be too noisy.

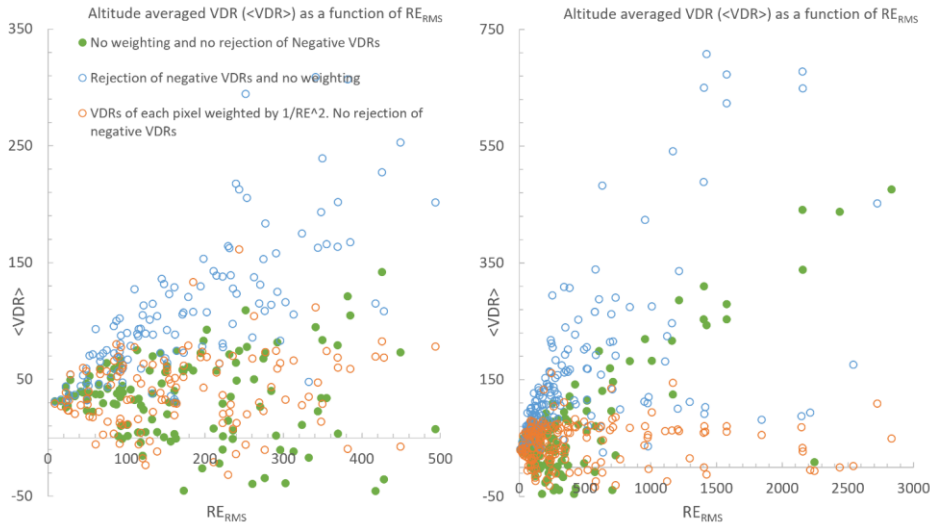
⁵⁸ too many values well above the typical VDR range for CM dust (see, for example, Fig. 1 of Tian et al., 2020).

⁵⁹ While retaining the rest of the (positive) VDR pixels in the given profile

⁶⁰ Simply put the exclusion of the negative values acted to increase the $\langle VDR \rangle$ values. This exclusion is debatable given that those negative values could well have a physical sense (they are likely associated with system constants whose range of variability could facilitate the production of negative VDR values for a fraction of the VDRs).

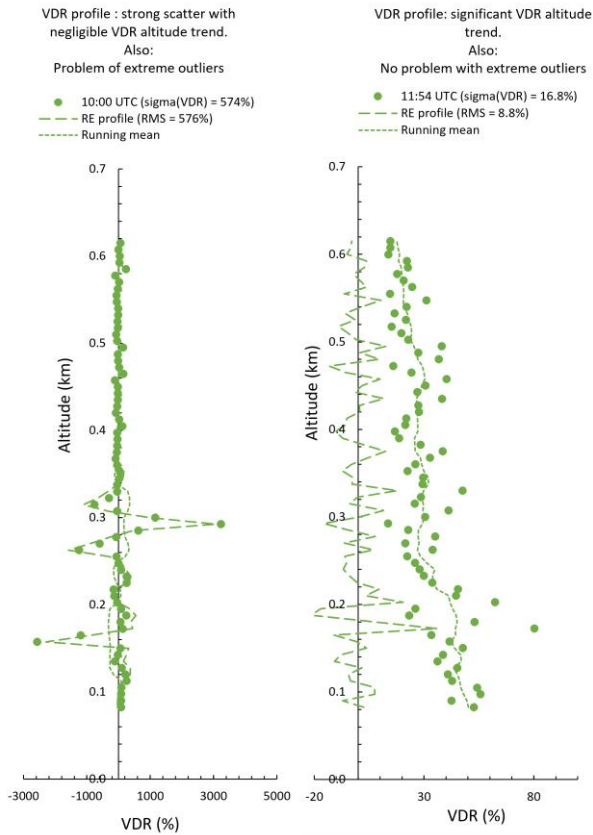
595 ○ The 2nd method includes a weighted mean of all VDRs in any given profile ($\langle VDR \rangle_\omega = \sum \omega VDR / \sum \omega$ where $\omega =$
 596 $1/RE^2$ for each profile pixel⁶¹. This takes all VDRs into consideration (does not suffer from the negative-VDR
 597 limitations) and seems to produce more realistic $\langle VDR \rangle$ values than the 1st method (values whose $\langle VDR \rangle$ range
 598 extends less into (both) the negative region and the positive region. Averaging in time (averaging over the event using
 599 an optical weighting factor of τ_β) would then be written as;

600
$$\langle \langle VDR \rangle_\omega \rangle_{\tau_\beta} = \sum \langle VDR \rangle_\omega \tau_\beta / \sum \tau_\beta \quad (A4)$$



601
 602 **Figure A2 – Altitude-averaged VDRs vs RMS residual errors (RE_{RMS}) for the July 23, 2007 dust event (the LH graph is a zoom of**
 603 **the RH graph). According to our notation, the orange-colored weighted averages should be labelled $\langle VDR \rangle_\omega$. These statistics were**
 604 **computed for the lidar altitude range from 82 to 615 m.**

⁶¹ The “ RE_{RMS} ” of the x axis in Fig. A2 represents the RMS residual error of the individual residual of any lidar pixel in any given vertical profile (the “individual residual” being the difference between a given VDR value at a given altitude and its running average; see the example for two representative lidar profiles in Fig. A3 below). This RE parameter enables an estimation of the noise magnitude by eliminating the systematic trend of the natural VDR variation. The inverse square weighting approach was inspired by standard texts on linear regression analysis (see, for example, Section 3.5 of Barford, 1967)



605

606

607

Figure A3 – Two representative lidar profiles (solid-shaded circles), their running mean (dotted curve) and their residual error (RE) difference (dashed curve).

608

A3.2: VDR weighting: profile-level impacts and resulting event-averaged statistics.

609

610

The impact of the ω weighting discussed in the previous sections is seen in Figures S1b to S7b⁶². In a nutshell the weighting significantly reduced the intra-profile standard deviations for all events (the bottom graphics of Figures S1b to S7b). We

⁶² Supplementary PowerPoint file “AHSRL_CIMEL_event_profiles”

611 would also argue that the event-wide average of the intra-profile standard deviation is the best candidate to describe the event-
 612 wide precision (noise) of our VDR estimates (see the Fig. S8 caption for details). On the other hand, the weighting introduced
 613 a significant amount of VDR variance in 2 events where very little variance existed prior to the weighting process (Events 1
 614 and 6 of Figures S1b and S6b)⁶³. The Event 1 and 6 standard deviations of intra-profile, event-level statistics that are
 615 summarized in the table of Fig. S8 are accordingly to be treated with caution. Indeed, the table shows explicitly that weighting
 616 did dramatically reduce the intra-profile standard deviations of all events excluding Events 1 and 6. We accordingly use the
 617 intra-profile statistics in the following section on the derivation of the PDRs for each event.

618 **A3.3: Estimation of the event-averaged CM PDR**

619 Figure A4 shows the event-averaged VDR and τ_β values for both the FM and CM components as a function of δ_{thr} (equation
 620 A3 above⁶⁴). The CM event averages are rather insensitive to small values of δ_{thr} (arguably because the weak PDR of the
 621 FM component and perhaps the weak DR of the sub- μm tail of the holistic CM PDR have little impact at small values of
 622 δ_{thr}). They only begin to rise when, we would argue, the sub- μm tail begins to play a more significant optical role (the larger
 623 DR of the sub- μm tail incites the beginning of a positive slope that starts to rise at δ_{thr} values ranging from 5 to 15%. A stable
 624 estimate of the dust PDR would occur at any value before the rises begin, say at $\delta_{thr} \sim 5\%$

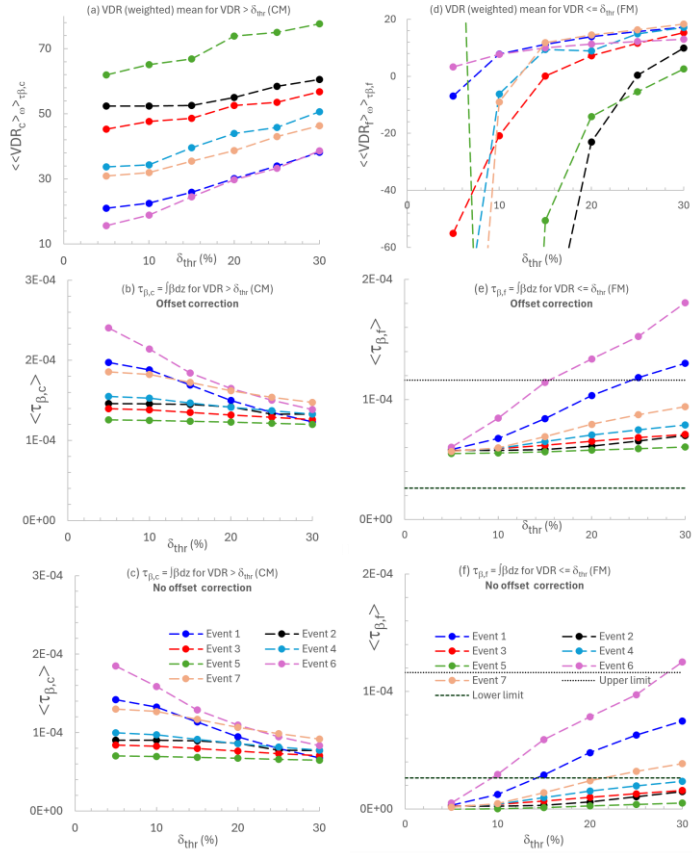
625 That 5% value was chosen to populate the event-dependent 532 nm PDR values of Table A1. Two of the Table A1 values
 626 are beyond the (780 nm) VDR upper limit for CM dust found, for example, in Fig. 1 of Tian et 2020 (their upper limit was ~
 627 50% for dust particles ranging in radius from ~ 1 to 5 μm)⁶⁵. On the other hand, all the Table A1 PDR values are largely
 628 contained within the 532 nm lidar ratio spread of “giant” near-source Saharan dust particles reported by Esselborn et al.
 629 (2009): their Fig. 9 lidar ratios vary between 40 and 60 sr for dust particles of volume median radii ranging from 4 to 15 μm
 630 (a spread that encompasses the 7 μm radius AERONET inversion dust peak that we report above in Fig. 3a). It should be
 631 emphasized that choices such as the (“ ω ”) weighting scheme and the optimal δ_{thr} value contain a level of subjective
 632 variability (in terms of, for example, the strengths of the weights applied). These factors and other sources of variability
 633 produce uncertainties that we estimate as being $\sim \pm$ the “ $\sigma(\text{PDR})$ ” values of Table A1.

⁶³ we could have reduced that variance with an appropriate smoothing approach but decided to forgo that added complication by the simple expedient of choosing the unweighted statistics since those statistics were largely free of the type of extreme VDR variation that one sees in the unweighted VDR means of Events 2, 3, 4, 5 and 7.

⁶⁴ to be mathematically precise, those CM event averages (the y axes labels of the LH graphs of Fig. A4) represent $\langle (VDR^{(VDR)\omega})_{\tau_\beta > \delta_{thr}} \rangle_{\omega}$ and $\langle \tau_\beta = \int \beta^{(VDR)\omega})_{\tau_\beta > \delta_{thr}} dz \rangle$ where the VDR vs δ_{thr} test is applied to each lidar pixel. The RH FM y-axis labels represent $\langle (VDR^{(VDR)\omega})_{\tau_\beta \leq \delta_{thr}} \rangle_{\omega}$ and $\langle \tau_\beta = \int \beta^{(VDR)\omega})_{\tau_\beta \leq \delta_{thr}} dz \rangle$

⁶⁵ Values which would tend to be moderately larger at 532 nm (see, for example, Table 1 of Mamouri & Ansmann, 2017)

634 The FM VDR averages are significantly more sensitive to δ_{thr} changes at smaller values of that parameter. This is due to a
635 combination of relatively small numbers of VDR pixels being available at small δ_{thr} values and the fact that there seemed to
636 be a small negative bias in the β values. The τ_β weighting across each event then produces wildly oscillating VDR averages
637 at δ_{thr} values of 5 and 10% (Event 2, 3, 4, 5 and 7 cases of Fig. A4d) that were enhanced by the very small τ_β weights in the
638 denominator of the weighting expression. The small negative bias was the cause of unrealistically small $\tau_{\beta,f}$ values for the
639 $\delta_{thr} = 5\%$ case in Fig. A4f. Adding a small β offset to all the β values produced the more realistic “Offset correction” values
640 of Fig. A4f (values that fit into a range of expected $\tau_{\beta,f}$ values between the horizontal dotted lines ; see the caption of Fig.
641 A4 for further details).



642
643
644
645
646

Figure A4 – VDR averaged results as a function of δ_{thr} for our 7 dust events. LH graphs (CM⁶⁶ for VDR values > δ_{thr}): (a) Altitude- and event-averaged VDR_c values (b) $\tau_{\beta,c}$ values with offset correction and (c) $\tau_{\beta,c}$ with no offset correction. RH graphs (d, e, f): the same array of graphs as the left-hand side but for the FM (VDR values $\leq \delta_{thr}$). The “offset correction” was a constant offset added on to β_c and β_f values to eliminate weakly negative β values (due, we presume, to a small calibration inconsistency). The “Lower

⁶⁶ the CM component of the “binary” model defined in Section A2 above

647 limit” and “Upper limit” are roughly-estimated expected bounds⁶⁷ on $\tau_{\beta_f}(0, L)$ (the FM backscatter optical depth across L). These
 648 statistics were computed for the lidar altitude range from 7.5 to 615 m (a more extensive range than that which was reported in the
 649 legend of Fig. A2; tests showed that the averaged VDR values were very similar in the face of such small changes in the profile
 650 range).

Event #	PDR(%)	$\sigma(\text{PDR})$ (%)
1	21	6
2	52	11
3	45	12
4	34	10
5	62	21
6	16	5
7	31	9

651
 652 **Table A1 – Dust PDRs for our 7 dust events ($\delta_{thr} = 5\%$). The event colors are consistent with Fig. A4. The precision estimates are**
 653 **event-averaged, intra profile standard deviations discussed in Section A3.2**

654 **A4: Does it help to perform a (ω) weighted CM and FM classification?**

655 If the VDR is so noisy that it requires weighting in the production of altitude-averaged VDRs then the question arises as to
 656 the variability of the VDR-dependent classification of CM and FM aerosols. An approach, which is arguably coherent with
 657 our VDR (residual error) weighting scheme, is to associate the VDR weights (which could be thought of as a “number of
 658 virtual pixels” that increase the importance attributed to a given lidar pixel). Our unweighted FM / CM backscatter AOD
 659 separation is, for the J^{th} lidar-profile at time $t_{i,J}$;

660
 661
$$\tau_{\beta_c} = \left(\sum_i \beta_{i,J}^{VDR_{i,J} \geq \delta_{thr}} \right) \Delta z \text{ and } \tau_{\beta_f} = \left(\sum_i \beta_{i,J}^{VDR_{i,J} < \delta_{thr}} \right) \Delta z \text{ where } \tau_{\beta_c} + \tau_{\beta_f} = \tau_{\beta} \quad (\text{A5})$$

662
 663 This equation explicitly indicates that the $\beta_{i,J}$ summations are mutually exclusive and carried out over all altitude bins of a
 664 given lidar profile. A weighted version of the FM and CM backscatter ODs for lidar profile J^{68} , is⁶⁹,

665
 666
$$\tau_{\beta_c}^{\omega} = K_J \left[\sum_i \omega_{i,J} \beta_{i,J} \right]^{VDR_{i,J} \geq \delta_{thr}} \Delta z \text{ and } \tau_{\beta_f}^{\omega} = K_J \left[\sum_i \omega_{i,J} \beta_{i,J} \right]^{VDR_{i,J} < \delta_{thr}} \Delta z \text{ where } \tau_{\beta}^{\omega} = \tau_{\beta_c}^{\omega} + \tau_{\beta_f}^{\omega} \quad (\text{A6})$$

⁶⁷ The extremes of 0PAL values of τ_f^0 computed for each event using a Eureka (experience-based) estimate of the optically active FM lidar backscatter region (~ 5 to 11 km) and the 0.615 km value of L (the atmospheric layer between 0PAL and PEARL).

⁶⁸ that takes into account the fact that all parameters (those enclosed in the square brackets) must be restricted by the FM and CM conditions

⁶⁹ where $\omega_{i,J}$ is the $1/RE^2$ weighting defined above

667

668 We then force the relation $\tau_{\beta c}^{\omega} + \tau_{\beta f}^{\omega} t o = \tau_{\beta}$ (this simply means that K_j is set to $\tau_{\beta}/\tau_{\beta}^{\omega}$). Dividing both sides by τ_{β} yields a
 669 familiar-looking CMF, FMF (CM fraction, FM fraction) type of relation:

670

$$671 \quad CMF^{\omega} + FMF^{\omega} = 1 \text{ where}^{70} \quad (A7a)$$

672

$$673 \quad CMF^{\omega} = \tau_{\beta c}^{\omega}/\tau_{\beta} \text{ and so } \tau_{\beta c}^{\omega} = \tau_{\beta} CMF^{\omega} \quad (A7b)^{71}$$

674

$$675 \quad FMF^{\omega} = \tau_{\beta f}^{\omega}/\tau_{\beta} \text{ and so } \tau_{\beta f}^{\omega} = FMF^{\omega}\tau_{\beta} \quad (A7c)$$

676

677 The $\tau_{\beta}^{\omega} = \tau_{\beta}$ forcing guarantees that the lidar-profile-integrated differences of $\Delta\tau_{\beta f} = \langle \tau_{\beta f} - \tau_{\beta f}^{\omega} \rangle$ and $\Delta\tau_{\beta c} = \langle \tau_{\beta c} - \tau_{\beta c}^{\omega} \rangle$
 678 of each profile cancel each other out ($\Delta\tau_{\beta f} + \Delta\tau_{\beta c} = 0$).

679 The results shown in Fig. A5 indicate that the “ ω ” weighting can effectively incite what we attribute to artificial $\Delta\tau_{\beta c}$ and
 680 $\Delta\tau_{\beta f}$ spikes⁷² (the lidar profiles show no corresponding anomalies), These spikes aside, the CM vs FM classification using a
 681 weighting approach generally showed no significant $\tau_{\beta c}^{\omega}$ vs $\tau_{\beta c}$ changes. Accordingly, any attempt to improve the quality of
 682 $\tau_{\beta c}$ by VDR-noise-based weighting results in either very little change or is the victim of significant outliers generated by the
 683 VDR weighting. Unlike the VDR weighting approach improvements (indicated by Fig. A2) there appears to be no significant
 684 advantage in a VDR-based filtering of the CM / FM classification.

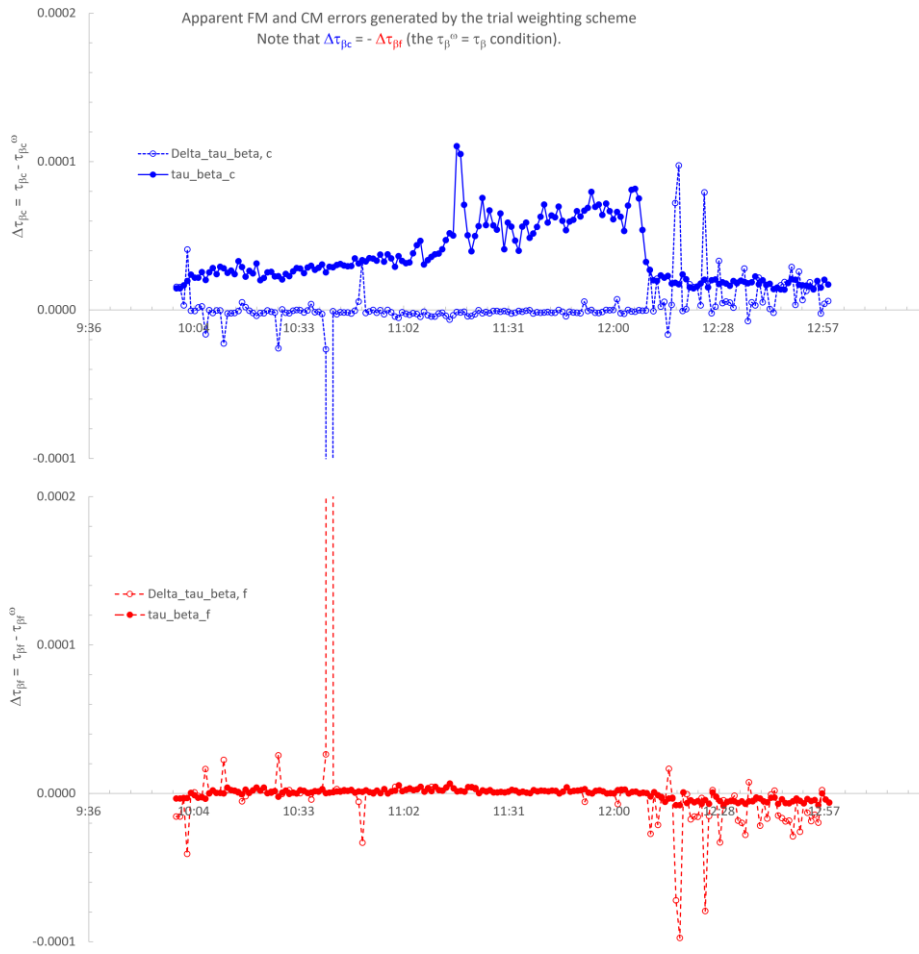
685

⁷⁰ Note that CMF^{ω} can be > 1 if $\tau_{\beta c}^{\omega} > \tau_{\beta}$ (negative β values from the real data and attendant underestimates of τ_{β} can wreak havoc with the “conservation of unity” equation)

⁷¹ A heuristic expression (showing explicitly that $0 \leq CMF^{\omega} \leq 1$) is;

$CMF^{\omega} = \tau_{\beta c}^{\omega}/\tau_{\beta}^{\omega} = \left[\sum_i \omega_{i,j} \beta_{i,j} \right]^{VDR_{i,j} \geq \delta_{thr}} \Delta z / \sum_i \omega_{i,j} \beta_{i,j} \Delta z = \left[\sum_i \omega_{i,j} \beta_{i,j} \right]^{VDR_{i,j} \geq \delta_{thr}} / \sum_i \omega_{i,j} \beta_{i,j}$. The explicit link with the unweighted stats is to employ τ_{β} when calculating $\tau_{\beta c}^{\omega}$ and $\tau_{\beta f}^{\omega}$ from CMF^{ω} .

⁷² The $\omega_{i,j} \beta_{i,j}$ weighting appears to enhance what would otherwise be nondescript points in the $\beta_{i,j}$ profile values.



686

687

688

Figure A5 - $\Delta\tau_{\beta c} = \langle \tau_{\beta c} - \tau_{\beta c}^{\text{FM}} \rangle$ vs time (top) and (b) $\Delta\tau_{\beta f} = \langle \tau_{\beta f} - \tau_{\beta f}^{\text{CM}} \rangle$ vs time (example of the July 23, 2007, event).

689 **Appendix B: Acronym and symbol glossary**

- 690 [AERONET: AErosol RObotic NETwork](#)
- 691 [AEROCAN: Canadian sub-network of AERONET](#)
- 692 [AHSRL: Arctic High Spectral Resolution Lidar](#)
- 693 [AOD: Aerosol Optical Depth](#)
- 694 [APS: Aerodynamic Particle Sizer](#)
- 695 [ASL: Above Sea Level](#)
- 696 [CAA: Canadian Arctic Archipelago](#)
- 697 [CARRA: Copernicus Arctic Regional ReAnalysis](#)
- 698 [CALIOP: Cloud-Aerosol Lidar with Orthogonal Polarization](#)
- 699 [CANDAC: Canadian Network for the Detection of Atmospheric Change](#)
- 700 [CM: Coarse Mode](#)
- 701 [CMF: Coarse Mode Fraction \(1-FMF\)](#)
- 702 [CW: ClockWise](#)
- 703 [CCW: CounterClockWise](#)
- 704 [DB: Deep Blue \(MODIS AOD retrieval algorithm over bright surfaces\)](#)
- 705 [DT: Dark Target \(MODIS AOD retrieval algorithm over dark targets \(water and vegetated land\)\)](#)
- 706 [DOD: Dust Optical Depth](#)
- 707 [DR: Depolarisation Ratio](#)
- 708 [ECCE: Environment and Climate Change Canada](#)
- 709 [FM: Fine Mode](#)
- 710 [FMF: Fine Mode Fraction \(MODIS product\)](#)
- 711 [HLD: High Latitude Dust](#)
- 712 [INP: Ice Nucleating Particle](#)
- 713 [IR: InfraRed](#)
- 714 [KLRS: Kluane Lake Research Station](#)
- 715 [MISR: Multi-angle Imaging SpectroRadiometer](#)
- 716 [MINX: MISR INteractive eXplorer](#)
- 717 [MODIS: Moderate Resolution Imaging Spectroradiometer](#)
- 718 [NA: Not Available](#)
- 719 [NASA: National Aeronautics and Space Administration](#)
- 720 [OD: Optical Depth](#)
- 721 [OPS: Optical Particle Sizer](#)

Formatted: French (Canada)

722 [PEARL: Polar Environment Atmospheric Research Laboratory](#)

723 [PMSD: Particle-Mass Size Distribution](#)

724 [PVSD: Particle-Volume Size Distribution](#)

725 [R: Correlation Coefficient](#)

726 [RS: Remote Sensing](#)

727 [STDstd: Standard Deviation](#)

728 [SWIR: Short-Wave InfraRed](#)

729 [UTC: Coordinated Universal Time](#)

730 [UV: UltraViolet](#)

731 [VDR: Volume Depolarization Ratio](#)

732 [WMO: World Meteorological Organization](#)

733 [\$\beta\$: Backscatter Coefficient](#)

734 [\$\beta_c\$: CM Lidar Backscatter Coefficient](#)

735 [\$\tau_\beta\$: Particulate Backscatter Optical Depth](#)

736 [\$\tau_{\beta,c}\$: CM \$\tau_\beta\$](#)

737 [\$\tau_{\beta,f}\$: FM \$\tau_\beta\$](#)

738 [\$\tau_c^L\$: Lidar CM AOD](#)

739 [\$\tau_c^F\$: Lidar FM AOD](#)

740 [\$\tau_c^O\$: OPAL CM AOD](#)

741 [\$\tau_{c,1.5}^O\$: OPAL cloud-screened \(L 1.5\) CM AOD](#)

742 [\$\tau_c^P\$: PEARL CM AOD](#)

743 [\$\tau_{c,1.5}^P\$: PEARL cloud-screened \(L 1.5\) CM AOD](#)

744 [\$S_c\$: CM Lidar Ratio](#)

745 [\$S_f\$: FM Lidar Ratio](#)

746 [\$v_\alpha\$: Particle-Volume Concentration](#)

747 [\$\delta_{thr}\$: VDR threshold](#)

748 [\$\Delta\tau_c\$: OPAL minus PEARL CM AOD difference \(\$\tau_c^O - \tau_c^P\$ \)](#)

749 [ws: Wind Speed \(km / h\)](#)

750 [OPAL: Zero Altitude PEARL Auxiliary Laboratory](#)

751 [AERONET: AErosol RObotic NETwork](#)

752 [AHSRL: Arctic High Spectral Resolution Lidar](#)

753 [AOD: Aerosol Optical Depth](#)

Formatted: English (Canada)

Formatted: English (Canada)

Formatted: English (Canada)

Formatted: English (Canada)

Formatted: English (Canada)

754 [APS: Aerodynamic Particle Sizer](#)
755 [ASL: Above Sea Level](#)
756 [CAA: Canadian Arctic Archipelago](#)
757 [CARRA: Copernicus Arctic Regional ReAnalysis](#)
758 [CALIOP: Cloud Aerosol Lidar with Orthogonal Polarization](#)
759 [CANDAC: Canadian Network for the Detection of Atmospheric Change](#)
760 [CM: Coarse Mode](#)
761 [CW: ClockWise](#)
762 [CCW: CounterClockWise](#)
763 [DB: Deep Blue \(MODIS AOD retrieval algorithm over bright surfaces\)](#)
764 [DT: Dark Target \(MODIS AOD retrieval algorithm over dark targets \(water and vegetated land\)\)](#)
765 [DOD: Dust Optical Depth](#)
766 [DR: Depolarisation Ratio](#)
767 [FM: Fine Mode](#)
768 [HLD: High Latitude Dust](#)
769 [MISR: Multi-angle Imaging SpectroRadiometer](#)
770 [MODIS: Moderate Resolution Imaging Spectroradiometer](#)
771 [NA: Not Available](#)
772 [PEARL: Polar Environment Atmospheric Research Laboratory](#)
773 [PMSD: Particle Mass Size Distribution](#)
774 [PVSD: Particle Volume Size Distribution](#)
775 [RS: Remote Sensing](#)
776 [\$v_g\$: Particle Volume Concentration](#)
777 [ws: Wind Speed \(km/h\)](#)
778 [OPAL: Zero Altitude PEARL Auxiliary Laboratory](#)

779 **6 Code availability**

780 MATLAB codes employed for computations reported in this manuscript can be obtained from Seyed Ali Sayedain
781 (seyed.ali.sayedain@usherbrooke.ca).

782 **7 Data availability**

783 AERONET data are available for download at <https://doi.org/10.17616/R3VK9T> (Lind and Gupta, 2023). The PEARL
784 AHSRL data are accessible from the University of Wisconsin HSRL data archives at
785 https://hsrl.ssec.wisc.edu/by_site/2/bscat/2007/07/ (last accessed: 2025-12-02). APS data can be obtained from Seyed Ali
786 Sayedain (seyed.ali.sayedain@usherbrooke.ca). ECCC hourly climate data for different stations can be downloaded at
787 <https://climate-change.canada.ca/climate-data/#/hourly-climate-data> (last accessed: 2025-12-02). MODIS Terra and Aqua
788 images and products along with MISR datasets can be downloaded from the Earth Science Data Systems (ESDS) at
789 <https://search.earthdata.nasa.gov/search>. Sentinel-2 data can be downloaded from Copernicus Browser
790 (<https://browser.dataspace.copernicus.eu/>). CARRA data at different levels (single, pressure, height and model) can be
791 downloaded from the Copernicus Climate Data Store (CDS) at <https://cds.climate.copernicus.eu/datasets>.

792 **8 Supplement**

793 The supplement related to this article is available online at: <https://doi.org/10.5281/zenodo.20561203>
794 <https://doi.org/10.5281/zenodo.17794333> (Sayedain and O'Neill, 20252026).

795 **9 Author contribution**

796 **Seyed Ali Sayedain:** Writing – original draft preparation – review & editing, Visualization, Investigation, Conceptualization,
797 Methodology, Formal analysis, Data curation, Validation, Software, Resources. **Norman T. O'Neill:** Writing – review &
798 editing, Supervision, Visualization, Conceptualization, Methodology, Formal analysis, Data curation, Validation, Funding
799 acquisition, Resources. **Keyvan Ranjbar:** Review & editing, Data curation, Resources. **Phillipe Gauvin-Bourdon:** Review
800 & editing, Data curation, Validation. **Rachel Chang:** Review & editing, Data curation, Validation, Funding acquisition,
801 Resources. **Patrick L. Hayes:** Review & editing, Data curation, Validation, Funding acquisition, Resources. **James King:**
802 Review & editing, Data curation, Validation, Funding acquisition.

803 **10 Competing interests**

804 The authors declare that they have no conflict of interest.

805 **11 Acknowledgements**

806 Valuable in-kind support was provided by the AEROCAN network of Environment and Climate Change Canada (ECCC), the
807 NASA AERONET network, the Canada Research Chairs Program (CRC), and the Canadian Network for the Detection of

808 Atmospheric Change (PAHA/CANDAC) team. We also acknowledge the use of imagery from the NASA Worldview
809 application (<https://worldview.earthdata.nasa.gov>), part of the NASA Earth Science Data and Information System (ESDIS).
810 We also acknowledge the use of Sentinel-2 data from the Copernicus Programme and MISR data provided by NASA. We
811 thank ESA and NASA for making these remote-sensing datasets freely accessible.

812 12 Financial support

813 was provided by the Discovery Grant (DG) program of the Natural Sciences and Engineering Research Council of Canada
814 (grant nos. RGPIN-2023-04943, RGPIN-2022-03785, RGPIN-2022-04963), the Canada Research Chairs Program (CRC-
815 2020-00285) and the SACIA-2 (Signatures of Aerosol-Cloud Interaction over the Arctic) project funded by the Canadian
816 Space Agency's ESS-DA (Earth System Science – Data Analysis) program (grant no. 21SUASACOA). SACIA-2 is a
817 collaborative project with Dalhousie University and the Université de Montréal.

818 References

- 819 AboEl-Fetouh, Y., O'Neill, N. T., Ranjbar, K., Hesarakı, S., Abboud, I., & Sobolewski, P. S.: Climatological-Scale
820 Analysis of Intensive and Semi-intensive Aerosol Parameters Derived From AERONET Retrievals Over the Arctic. *Journal*
821 *of Geophysical Research: Atmospheres*, 125(10). <https://doi.org/10.1029/2019jd031569>, 2020.
- 822 Arnalds, O.: Dust sources and deposition of aeolian materials in Iceland. *Icelandic Agricultural Sciences*, 23, 3–21.
823 https://www.moldin.net/uploads/3/9/3/3/39332633/olafur_arnalds_2010_ias.pdf (accessed: 2025-11-22), 2010.
- 824 Adams, P., & Dunbar, M.: Arctic Archipelago. In *The Canadian Encyclopedia*. Available at:
825 <https://www.thecanadianencyclopedia.ca/en/article/arctic-archipelago> (last accessed: 2025-11-22), 2015.
- 826 Bachelder, J., Cadieux, M., Liu-Kang, C., Lambert, P., Filoche, A., Galhardi, J. A., Hadioui, M., Chaput, A., Bastien-
827 Thibault, M. P., Wilkinson, K. J., King, J., & Hayes, P. L.: Chemical and microphysical properties of wind-blown dust near
828 an actively retreating glacier in Yukon, Canada. *Aerosol Science and Technology*, 54(1), 2–20.
829 <https://doi.org/10.1080/02786826.2019.1676394>, 2020.
- 830 Baddock, M., Hall, A., Rideout, J., Bryant, R., Bullard, J., & Gassó, S.: Satellite observations of Arctic blowing dust events
831 >82°N. *Weather*, 1–6. <https://doi.org/10.1002/wea.7617>, 2024.
- 832 Barford, N. C., Experimental measurements: precision, error and truth, Addison-Wesley Publishing Company, Inc., Don
833 Mills, Ontario, ISBN 10: 0201003953, ISBN 13: 9780201003956, 1967.
- 834 Barr, S. L., Wyld, B., McQuaid, J. B., Neely Iii, R. R., & Murray, B. J.: Southern Alaska as a source of atmospheric mineral
835 dust and ice-nucleating particles, *Sci. Adv.*, 9, eadg3708. <https://doi.org/10.1126/sciadv.adg3708>, 2023.

836 Bullard, J. E., Matthew, B., Tom, B., John, C., Eleanor, D., Diego, G., Santiago, G., Gudrun, G., Richard, H., Robert, M.,
837 Cheryl, M.-N., Tom, M., Helena, S., & Thorsteinsson, T.: High latitude dust in the Earth system, *Rev. Geophys.*, 54, 447–485.
838 <https://doi.org/10.1002/2016RG000518>, 2016.

839 Eloranta, E. W., I. A. Razenkov, J. P. Garcia, & J. Hedrick, -, 22nd International Laser Radar Conference, July 12–16,
840 Matera, Italy, 2004.

841 Dörnbrack, A., Stachlewska, I. S., Ritter, C., & Neuber, R.: Aerosol distribution around Svalbard during intense easterly
842 winds. *Atmospheric Chemistry and Physics*, 10(4), 1473–1490. <https://doi.org/10.5194/ACP-10-1473-2010>, 2010.

843 Dubovik, O., Holben, B., Eck, T. F., Smirnov, A., Kaufman, Y. J., King, M. D., Tanré, D., & Slutsker I.: Variability of
844 absorption and optical properties of key aerosol types observed in worldwide locations. *Journal of the atmospheric sciences*.
845 59(3):590–608. [https://doi.org/10.1175/1520-0469\(2002\)059<0590:VOAAOP>2.0.CO;2](https://doi.org/10.1175/1520-0469(2002)059<0590:VOAAOP>2.0.CO;2), 2002.

846 Esselborn, M., Wirth, M., Fix, A., Weinzierl, B., Rasp, K., Tesche, M., & Petzold, A.: Spatial distribution and optical
847 properties of Saharan dust observed by airborne high spectral resolution lidar during SAMUM 2006. *Tellus B Chem. Phys.*
848 *Meteorol.* 61, 131–143. <https://doi.org/10.1111/j.1600-0889.2008.00394.x>, 2009.

849 Garay, M. J., Witek, M. L., Kahn, R. A., Seidel, F. C., Limbacher, J. A., Bull, M. A., Diner, D. J., Hansen, E. G.,
850 Kalashnikova, O. V., Lee, H., Nastan, A. M., & Yu, Y.: Introducing the 4.4 km spatial resolution Multi-Angle Imaging
851 SpectroRadiometer (MISR) aerosol product, *Atmos. Meas. Tech.*, 13, 593–628. <https://doi.org/10.5194/amt-13-593-2020>,
852 2020.

853 Giles, D. M., Sinyuk, A., Sorokin, M. G., Schafer, J. S., Smirnov, A., Slutsker, I., Eck, T. F., Holben, B. N., Lewis, J. R.,
854 Campbell, J. R., Welton, E. J., Korkin, S. V., & Lyapustin, A. I.: Advancements in the Aerosol Robotic Network (AERONET)
855 Version 3 database – automated near-real-time quality control algorithm with improved cloud screening for Sun photometer
856 aerosol optical depth (AOD) measurements, *Atmos. Meas. Tech.*, 12, 169–209. <https://doi.org/10.5194/amt-12-169-2019>,
857 2019.

858 Groot Zwaafink, C. D., Grythe, H., Skov, H., & Stohl, A.: Substantial contribution of northern high-latitude sources to
859 mineral dust in the Arctic, *J. Geophys. Res.*, 121, 13678–13697. <https://doi.org/10.1002/2016JD025482>, 2016.

860 Hansen J. E. and Travis L. D.: Light scattering in planetary atmospheres, *Space science reviews*. 16(4):527–610.
861 <https://doi.org/10.1007/BF00168069>, 1974.

862 Huang, Y., Adebisi, A. A., Formenti, P., & Kok, J. F.: Linking the different diameter types of aspherical desert dust
863 indicates that models underestimate coarse dust emission. *Geophysical Research Letters*, 48, e2020GL092054.
864 <https://doi.org/10.1029/2020GL092054>, 2021.

865 Justice, C. O., Townshend, J. R. G., Vermote, E. F., Masuoka, E., Wolfe, R. E., Saleous, N., Roy, D. P., & Morisette, J. T.:
866 An overview of MODIS Land data processing and product status. *Remote Sensing of Environment*, 83(1–2), 3–15.
867 [https://doi.org/10.1016/S0034-4257\(02\)00084-6](https://doi.org/10.1016/S0034-4257(02)00084-6), 2002.

868 Kahn, R. A., Li, W.-H., Moroney, C., Diner, D. J., Martonchik, J. V., & Fishbein, E.: Aerosol source plume physical

869 characteristics from space-based multiangle imaging, *Journal of Geophysical Research Atmospheres*, 112, D11205.
870 <https://doi.org/10.1029/2006JD007647>, 2007.

871 Kaltschmitt, M., Streicher, W., & Wiese, A.: *Renewable Energy – Technology, Economics and Environment (XXXII)*.
872 Berlin, Heidelberg, New York, Springer. ISBN 3-540-70947-9, ISBN 978-3-540-70947-3, Page 55. Available at:
873 <http://www.springer.com/us/book/9783540709473> (last accessed: 2025-11-22), 2007.

874 Kawai, K., Matsui, H., & Tobo, Y.: Dominant Role of Arctic Dust With High Ice Nucleating Ability in the Arctic Lower
875 Troposphere. *Geophysical Research Letters*, 50(8), 1–10. <https://doi.org/10.1029/2022GL102470>, 2023.

876 Lesins, G., Duck, T. J., & Drummond, J. R.: Climate trends at Eureka in the Canadian high arctic. *Atmosphere-*
877 *Ocean*, 48(2), 59–80. <https://doi.org/10.3137/AO1103.2010>, 2010.

878 Levy, R., Hsu, C., et al., : MODIS Atmosphere L2 Aerosol Product. NASA MODIS Adaptive Processing System, Goddard
879 Space Flight Center, USA: http://dx.doi.org/10.5067/MODIS/MOD04_3K.061, 2015a.

880 Levy, R., Hsu, C., et al., : MODIS Atmosphere L2 Aerosol Product. NASA MODIS Adaptive Processing System, Goddard
881 Space Flight Center, USA: http://dx.doi.org/10.5067/MODIS/MYD04_3K.061, 2015b.

882 Levy, R., Hsu, C., et al., : MODIS Atmosphere L2 Aerosol Product. NASA MODIS Adaptive Processing System, Goddard
883 Space Flight Center, USA: http://dx.doi.org/10.5067/MODIS/MOD04_L2.061, 2015c.

884 Levy, R., Hsu, C., et al., : MODIS Atmosphere L2 Aerosol Product. NASA MODIS Adaptive Processing System, Goddard
885 Space Flight Center, USA: http://dx.doi.org/10.5067/MODIS/MYD04_L2.061, 2015d.

886 Lind, E. and Gupta, P.: AERONET, Registry of Research Data Repositories [data set]. <https://doi.org/10.17616/R3VK9T>
887 (last accessed: 2025-12-02), 2023.

888 Liu, Z., Fairlie, T. D., Uno, I., Huang, J., Wu, D., Omar, A., Kar, J., Vaughan, M., Rogers, R., Winker, D., Trepte, C., Hu,
889 Y., Sun, W., Lin, B., & Cheng, A.: Transpacific transport and evolution of the optical properties of Asian dust, *Journal of*
890 *Quantitative Spectroscopy & Radiative Transfer*, 116, 24–33. <https://doi.org/10.1016/j.jqsrt.2012.11.011>, 2013.

891 Mamouri, R. E. & Ansmann, A.: Fine and coarse dust separation with polarization lidar, *Atmos. Meas. Tech.*, 7, 3717–
892 3735. <https://doi.org/10.5194/amt-7-3717-2014>, 2014.

893 Mamouri, R. E. & Ansmann, A.: Potential of polarization/Raman lidar to separate fine dust, coarse dust, maritime, and
894 anthropogenic aerosol profiles, *Atmos. Meas. Tech.*, 10, 3403–3427. <https://doi.org/10.5194/amt-10-3403-2017>, 2017.

895 Martonchik, J. V., Diner, D. J., Kahn, R. A., Ackerman, T. P., Verstraete, M. M., Pinty, B., & Gordon, H. R.: Techniques
896 for the retrieval of aerosol properties over land and ocean using multiangle imaging. *IEEE Transactions on Geoscience and*
897 *Remote Sensing*, 36(4), 1212–1227. <https://doi.org/10.1109/36.701027>, 1998.

898 Meinander, O., Dagsson-Waldhauserova, P., Amosov, P., Aseyeva, E., Atkins, C., Baklanov, A., Baldo, C., Barr, S. L.,
899 Barzycka, B., Benning, L. G., Cvetkovic, B., Enchilik, P., Frolov, D., Gassó, S., Kandler, K., Kasimov, N., Kavan, J., King,
900 J., Koroleva, T., Krupskaya, V., Kulmala, M., Kusiak, M., Lappalainen, H. K., Laska, M., Lasne, J., Lewandowski, M., Luks,
901 B., McQuaid, J. B., Moroni, B., Murray, B., Möhler, O., Nawrot, A., Nickovic, S., O'Neill, N. T., Pejanovic, G., Popovicheva,

902 O., Ranjbar, K., Romanias, M., Samonova, O., Sanchez-Marroquin, A., Schepanski, K., Semenov, I., Sharapova, A.,
903 Shevnina, E., Shi, Z., Sofiev, M., Thevenet, F., Thorsteinsson, T., Timofeev, M., Umo, N. S., Uppstu, A., Urupina, D., Varga,
904 G., Werner, T., Arnalds, O., & Vukovic Vimic, A.: Newly identified climatically and environmentally significant high-latitude
905 dust sources. *Atmospheric Chemistry and Physics*, 22(17), 11889–11930. <https://doi.org/10.5194/acp-22-11889-2022>, 2022.

906 Met Office, Beaufort, National Meteorological Library and Archive, Fact sheet 6 – The Beaufort Scale. Available at:
907 <https://www.metoffice.gov.uk/binaries/content/assets/metofficegovuk/pdf/research/library-and->
908 [archive/library/publications/factsheets/factsheet_6-the-beaufort-scale_2023.pdf](https://www.metoffice.gov.uk/binaries/content/assets/metofficegovuk/pdf/research/library-and-archive/library/publications/factsheets/factsheet_6-the-beaufort-scale_2023.pdf) (last accessed: 2025-11-22), 2010.

909 Mishchenko, M. I., & Sassen, K.: Depolarization of lidar returns by small ice crystals: An application to contrails,
910 *Geophysical Research Letters*, 25(3), 309–312. <https://doi.org/10.1029/97GL03764>, 1998.

911 MISR Handbook: Multi-angle Imaging SpectroRadiometer Project Handbook, *Atmospheric Science Data Center*, NASA
912 Langley Research Center. Available at: https://asdc.larc.nasa.gov/documents/misr/guide/misr_ov2.pdf (last accessed: 2024-
913 12-21), 2000.

914 Nelson, D. L., Garay, M. J., Kahn, R. A., & Dunst, B. A.: Stereoscopic height and wind retrievals for aerosol plumes with
915 the MISR INteractive eXplorer (MINX). *Remote Sensing*, 5(9), 4593–4628. <https://doi.org/10.3390/rs5094593>, 2013.

916 O'Neill, N. T., Ranjbar, K., Ivănescu, L., Blanchard, Y., Sayedain, S. A., & AboEl-Fetouh, Y.: Remote-sensing
917 detectability of airborne Arctic dust, *Atmos. Chem. Phys.*, 25, 27–44, <https://doi.org/10.5194/acp-25-27-2025>, 2025.

918 Ranjbar, K., O'Neill, N. T., Ivanescu, L., King, J., & Hayes, P. L.: Remote sensing of a high-Arctic, local dust event over
919 Lake Hazen (Ellesmere Island, Nunavut, Canada). *Atmospheric Environment*, 246, 118102.
920 <https://doi.org/10.1016/j.atmosenv.2020.118102>, 2021.

921 Remer, L. A., Mattoo, S., Levy, R. C., & Munchak, L. A.: MODIS 3 km aerosol product: algorithm and global perspective,
922 *Atmos. Meas. Tech.*, 6, 1829–1844. <https://doi.org/10.5194/amt-6-1829-2013>, 2013.

923 Sayedain, S. A., O'Neill, N. T., King, J., Hayes, P. L., Bellamy, D., Washington, R., Engelstaedter, S., Vicente-Luis, A.,
924 Bachelder, J., & Bernhard, M.: Detection and analysis of Lhù'ààn Man' (Kluane Lake) dust plumes using passive and active
925 ground-based remote sensing supported by physical surface measurements. *Atmospheric Measurement Techniques*, 16(17),
926 4115–4135. <https://doi.org/10.5194/amt-16-4115-2023>, 2023.

927 Sayedain, S. A., & O'Neill, N. T.: Remote sensing of local-dust across the Canadian Arctic - Supplementary Material. In
928 *Atmospheric Measurement Techniques*. Zenodo. <https://doi.org/10.5281/zenodo.20561203>,
929 <https://doi.org/10.5281/zenodo.17794333>, 2025

930 Sayer, A. M., Munchak, L. A., Hsu, N. C., Levy, R. C., Bettenhausen, C., & Jeong, M.-J.: MODIS Collection 6 aerosol
931 products: Comparison between Aqua's e-Deep Blue, Dark Target, and “merged” data sets, and usage recommendations,
932 *Journal of Geophysical Research: Atmospheres.*, 119, 13,965–13,989. <https://doi.org/10.1002/2014JD022453>, 2014.

933 Sayer, A., Personal communication, 2025.

934 Sinyuk, A., Holben, B. N., Eck, T. F., Giles, D. M., Slutsker, I., Korokin, S., Schafer, J. S., Smirnov, A., Sorokin, M., &
935 Lyapustin, A.: The AERONET Version 3 aerosol retrieval algorithm, associated uncertainties and comparisons to Version 2.
936 Atmospheric Measurement Techniques. Jun 26;13(6):3375–411. <https://doi.org/10.5194/amt-13-3375-2020>, 2020.

937 Song, Q., Zhang, Z., Yu, H., Ginoux, P., & Shen, J.: Global dust optical depth climatology derived from CALIOP and
938 MODIS aerosol retrievals on decadal timescales: regional and interannual variability, Atmos. Chem. Phys., 21, 13369–13395.
939 <https://doi.org/10.5194/acp-21-13369-2021>, 2021.

940 Tian, Y., Pan, X., Wang, Z., Wang, D., Ge, B., Liu, X., Zhang, Y., Liu, H., Lei, S., Yang, T., Fu, P., Sun, Y., & Wang, Z.:
941 Transport patterns, size distributions, and depolarization characteristics of dust particles in East Asia in spring 2018, Journal
942 of Geophysical Research: Atmospheres, 125(16):e2019JD031752. <https://doi.org/10.1029/2019JD031752>, 2020.

943 Tobo, Y., Adachi, K., DeMott, P. J., Hill, T. C. J., Hamilton, D. S., Mahowald, N. M., Nagatsuka, N., Ohata, S., Uetake,
944 J., Kondo, Y., & Koike, M.: Glacially sourced dust as a potentially significant source of ice nucleating particles. *Nature*
945 *Geoscience*, 12(4), 253–258. <https://doi.org/10.1038/s41561-019-0314-x>, 2019.

946 TSI Incorporated, *Aerodynamic Particle Sizer® (APS™) Model 3321* [Specification sheet]. Available at:
947 <https://www.tsi.com/getmedia/7fd20aa0-8540-4b8d-8572-d164366dd08c/3321-Spec-Sheet-US?ext=.pdf> (last
948 accessed: 2025-01-11), 2022.

949 Uno, I., Eguchi, K., Yumimoto, K., Takemura, T., Shimizu, A., Uematsu, M., Liu, Z., Wang, Z., Hara, Y., & Sugimoto,
950 N.: Asian dust transported one full circuit around the globe. *Nature Geoscience*, 2(8), 557–560.
951 <https://doi.org/10.1038/ngeo583>, 2009.

952 Weitkamp, C.: Lidar: range-resolved optical remote sensing of the atmosphere, Springer Science & Business Media, New
953 York (HSRL chapter 5 by E. Eloranta), 2005.

954 Williamson, M. -C. & MacRae, R. A.: Mineralization potential in volcanic rocks of the Strand Fiord Formation and
955 associated intrusions, Axel Heiberg Island, Nunavut, Canada. Geological Survey of Canada, Open File, 7981, 34. Natural
956 Resources Canada. <https://doi.org/10.4095/297365>, 2015.

957 Witek, M. L., Garay, M. J., Diner, D. J., Bull, M. A., Seidel, F. C., Nastan, A. M., & Hansen, E. G.: Introducing the MISR
958 level 2 near real-time aerosol product. *Atmospheric Measurement Techniques*, 14(8), 5577–5591. [https://doi.org/10.5194/amt-](https://doi.org/10.5194/amt-14-5577-2021)
959 [14-5577-2021](https://doi.org/10.5194/amt-14-5577-2021), 2021.

960 Woo, M. K., Edlund, S. A., & Young, K. L.: Occurrence of early snow-free zones on Fosheim Peninsula, Ellesmere Island,
961 Northwest Territories. *Current Research, Part B, Geological Survey of Canada Paper*, 91, 9-14, ISBN: 0-660-56282-0.
962 Available at: https://publications.gc.ca/collections/collection_2017/rncan-nrcan/M44-91-1B.pdf (last accessed: 2025-11-22),
963 1991.

964 Xi, Y., Xu, C., Downey, A., Stevens, R., Bachelder, J. O., King, J., Hayes, P. L., & Bertram, A. K.: Ice nucleating properties
965 of airborne dust from an actively retreating glacier in Yukon, Canada. *Environmental Science: Atmospheres*, 2(4), 714–726.
966 <https://doi.org/10.1039/d1ea00101a>, 2022.

967 Yang, S., Preißler, J., Wiegner, M., von Löwis, S., Petersen, G. N., Parks, M. M., & Finger, D. C.: Monitoring dust events
968 using doppler lidar and ceilometer in Iceland. *Atmosphere*, 11(12), 1–23. <https://doi.org/10.3390/atmos11121294>, 2020.

969 Zhao, X., Huang, K., Fu, J. S., & Abdullaev, S. F.: Long-range transport of Asian dust to the Arctic: identification of
970 transport pathways, evolution of aerosol optical properties, and impact assessment on surface albedo changes. *Atmospheric*
971 *Chemistry and Physics*, 22(15), 10389–10407. <https://doi.org/10.5194/acp-22-10389-2022>, 2022.